IPP-Report

MAX-PLANCK-INSTITUT
FÜR PLASMAPHYSIK

Kiwoo Lee

Power Load Investigation in Negative Triangularity ASDEX Upgrade

IPP 2023-12
Dezember 2023



Master Thesis in Physics at
Technische Universität München

Power Load Investigation in Negative Triangularity ASDEX Upgrade

presented by

Kiwoo Lee

München, 15.11.2022

First Promoter: Prof. Dr. Ulrich Stroth

Second Promoter: Prof. Dr. Rudolf Neu

Supervisor: Dr. Michael Faitsch

Abstract

Nuclear fusion is one of the green energy sources and one of the technologies that mankind must achieve. So far, nuclear fusion research has been aimed at high temperature, high density, and long confinement time. One of the next steps in fusion research is power exhaust. During the nuclear fusion operation, not all of the energy is confined. Some of it escapes its confinement and is exhausted. Power load onto the plasma-facing components is one of the major challenges for a future thermonuclear fusion reactor. Even though power loads into the divertor are acceptable for current devices, this will not be true for future fusion devices. Among various measures to prepare for this, negative triangularity operation has emerged as an alternative and recently got attention. However, there have been few studies on heat exhaust. This thesis reports on the first power loads study in ASDEX Upgrade negative triangularity scenario.

Using infrared thermography, the power falling on the divertor, the region in a tokamak design for the strongest plasma-wall interaction, is studied, focusing on the key parameter called power fall-off length λ_q. First, the impact on λ_q of various plasma parameters is examined, including total heating power and poloidal magnetic field strength. The difference between toroidal magnetic field directions is compared with each other. Negative triangularity shots are compared with other scenarios, which have different triangularity but similar input parameters, to find out the influence of shaping. Moreover, consistency with the published scaling laws is checked.

As a result, there was no clear dependence on poloidal magnetic field strength. In the reversed toroidal magnetic field discharges, λ_q shows an about proportional correlation with total heating power. Especially a considerable difference in fall-off length between the two toroidal magnetic fields is observed with a factor of two smaller values in the reversed toroidal magnetic field. More specifically, λ_q in reversed field direction regime is around 1.5 mm, and in the normal field direction regime is about 3 mm. In addition, negative triangularity shots have the same or smaller λ_q than other scenarios. The comparisons to published scaling laws and a drift-based model reveal that in normal toroidal field direction, satisfactory agreement is observed. However, in the case of reversed toroidal magnetic field direction, the predictions are significantly too large.

This first power exhaust study in ASDEX Upgrade negative triangularity scenario reveals that a potential future device might need to consider smaller λ_q values than the mostly used scaling law prediction when operating in the reversed magnetic field configuration.

Contents

Chapter 1

Introduction

1.1 Motivation and Nuclear Fusion

Nuclear fusion is a reaction in which two or more atomic nuclei combine into one or more different atomic nuclei and subatomic particles. The fusion reaction releases energy as a mass defect from the difference in the binding energy of nuclei. Even though the idea of using fusion energy was introduced around the same time as nuclear fission, fusion technology is not completed and is still being studied. One of the fusion reactions is the deuterium and tritium reaction which is the most promising on earth. Since this reaction does not have carbon dioxide byproducts and safety risks like nuclear fission plants, it can be classified as green energy. Moreover, deuterium is abundant on earth. Tritium can be bread from lithium, so fuel for this fusion reaction is easy to obtain. Further, fuel efficiency is higher than other energy sources. For these reasons, nuclear fusion energy received attention as a solution to the energy demand of humankind and became one of the technologies that must be achieved.
The most studied and developed fusion is thermonuclear fusion, confinement by magnetic fields. The fusion reaction requires high pressure and high temperature, so on earth magnetic confinement allows a reactor to operate without touching the surrounding to achieve those conditions. For a thermonuclear fusion reaction in magnetic confinement, the fuel has to be heated to 150 million K. The fuel particles with high energy at this temperature are fully ionized and become plasma. The plasma is confined into a magnetic field using Lorentz force. So far, nuclear fusion research has been aimed at achieving high temperature, high density, and long confinement time. A self-sustained plasma without external heating is named "ignited". The ignition condition for the D-T fusion is achieved when the alpha particle in the fusion reaction compensates the loss power [Wesson and Campbell, 2011].

$$nT\tau_E > 3 \times 10^{21}\,\mathrm{m}^{-3}\mathrm{keVs} \tag{1.1}$$

It is calculated as a triple product of the main parameters of fusion plasma where n density, T temperature, and τ_E energy confinement time [Eq. 1.1].

1.2 Tokamak Device

The beginning of studying magnetic confinement fusion was a linear pinch device that applies magnetic flux with both open ends [Haines et al., 2000]. Nevertheless, particles kept going out at both ends, and to prevent them from escaping, the fusion device continued to develop and attached both ends to form a torus shape. The tokamak device has a bent toroidal magnetic field without open ends. This magnetic field inside the tokamak has a $1/R$ dependence, with R being the major radius. As a result of the bent magnetic field, the particles separate by charges due to drifts and drift in the radial direction with the electric field created by this charge separation [Section. 2.3.1]. A poloidal field is added to compensate for this. These main sets of magnetic field coils have become primary components of the tokamak device. In Fig. 1.1,

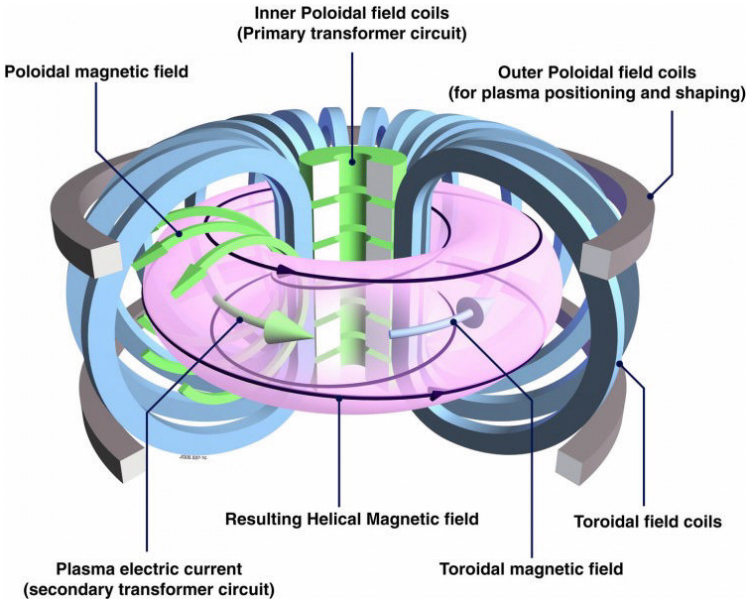

FIGURE 1.1: Basic structure and magnetic coil system of a tokamak. Retrieved from [euro-fusion.org, 2011].

a schematic of a tokamak is shown. The configuration of the tokamak device consists of 'D'-shaped toroidal field coils shown in blue, generating the toroidal magnetic field, and outer poloidal field coils limiting the horizontal movement of the plasma as well as position control. These coils and magnetic fields each have different effects, and with all together, stable magnetic confinement is achieved. In addition, the current tokamak experiments consist of external heating sources as well as various diagnostic systems for research.

1.3 Divertor

With the magnetic configuration described in the previous section, nested flux surfaces are created. Charged particles move freely along these magnetic field

lines. However, these flux surfaces ultimately intersect solid material walls. High energy particles induce damage to plasma-facing materials, and impurities from plasma-wall interaction cause poor confinement. Plasma in the tokamak has to avoid contact with surrounding walls. A dedicated area is introduced where the plasma-wall interaction takes place. This area is called the limiter. The limiter configuration limits plasma volume by the intersection with the surrounding structure. Fig. 1.2 (left) shows a poloidal cross-section

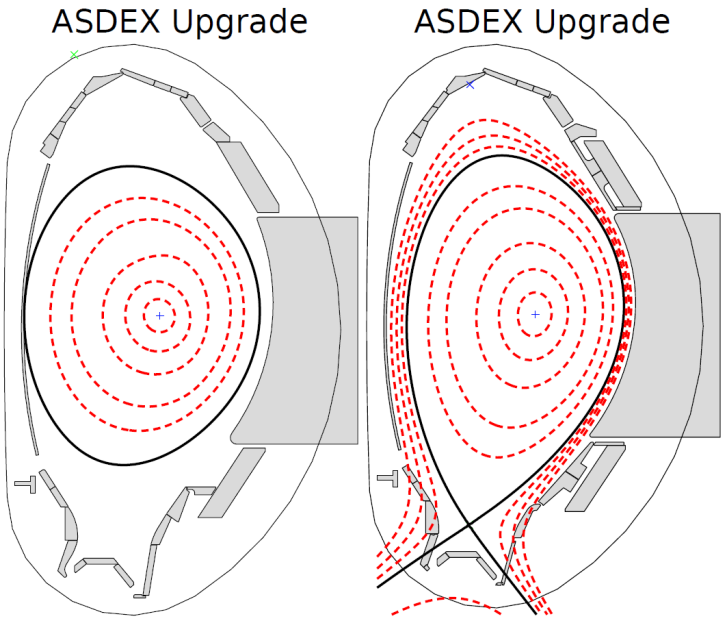

FIGURE 1.2: Poloidal cross-section of ASDEX Upgrade. The black line represents (left) Last closed flux surface and (right) separatrix as the boundary of the confined region. Retrieved from [Faitsch, 2017]

of ASDEX Upgrade with such a magnetic field configuration. The black line depicts the last closed flux surface (LCFS) as the outermost flux surface that does not intersect the surrounding material but closes within itself without wall interaction. The volume inside the LCFS is called the core or confined region. In contrast, field lines outside the LCFS are called the scrape-off layer (SOL) and intersect with solid material. In the early time, the tokamak experiments operated with a limiter configuration. However, sputtered wall material causes impurities that enter the core plasma and lower the confinement efficiency. In order to compensate for this phenomenon, a divertor configuration was introduced. The divertor collects the SOL particles to a specific location and structurally prevents the sputtered particles from going to the plasma core. In other words, the divertor is further separated from the core plasma as the limiter and hence strongly reduces the influx of impurities. For the divertor configuration, the shape of the magnetic flux is changed with an additional magnetic field. A toroidal current is applied anti-parallel to the plasma current, reducing the poloidal magnetic field and creating a point with

zero poloidal magnetic field strength, called X-point. According to the location of the X-point, it is called lower single null (LSN) and upper single null (USN) configuration. Fig. 1.2 (right) shows a poloidal cross-section of ASDEX Upgrade with such a LSN configuration. The solid, black line is called the separatrix. The field lines in the SOL are deflected into the divertor. Due to the strong particle and heat fluxes, the divertor is equipped with components designed to maximize resilience. Therefore, the divertor is made using a strong material against heat to withstand particle flux and heat flux that come out to SOL. In the case of ASDEX Upgrade (AUG), tungsten and tungsten-coated carbon are used [Neu et al., 2002].

1.4 Scenarios

After using divertor configuration in tokamak devices, the high-energy confinement mode (H-mode) was discovered in the first diverted tokamak, ASDEX [Wagner et al., 1982]. After H-mode was discovered, the confinement regimes before H-mode were named low-confinement mode (L-mode). H-mode

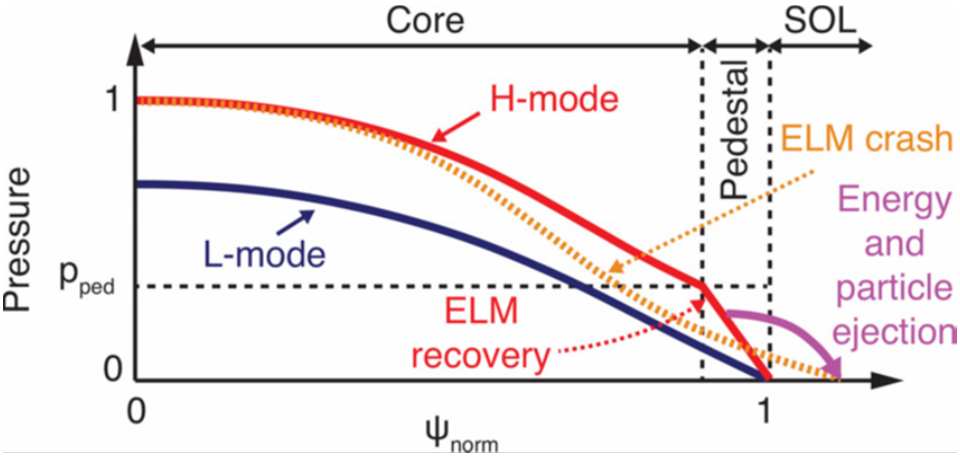

FIGURE 1.3: Sketch of L- and H-mode pressure profiles across the minor radius. The H-mode profile shows a steep gradient at the edge, the pedestal. Edge localized mode periodically relaxes this pedestal. Retrieved from [Lampert et al., 2022]

regimes achieved higher energy confinement and particle confinement time by a factor of two than L-mode by having steep edge density and temperature profiles [Wagner et al., 1982, Wagner et al., 1985] [Fig. 1.3]. In H-mode, steep edge profiles are established because of an edge transport barrier (ETB), called pedestal. However, this steep pressure gradient provides a source of free energy for instabilities. A periodic relaxation of the pedestal profiles is observed in H-mode. These events are named edge localized modes (ELMs) [Zohm, 1996]. Various types of ELMs exist, with the most studied being type-I ELMs. These type-I ELMs cause an enormous amount of particle and heat flux into the divertor [Loarte et al., 2003]. In recent years the impact of these ELMs has

been extensively studied, concluding that naturally occurring type-I ELMs are likely unacceptable in future fusion power plants [Loarte et al., 2003, Eich et al., 2017]. In order to avoid type-I ELM, other operational regimes are developed. Improved energy-confinement mode (I-mode) [Whyte et al., 2010] and enhanced D alpha H-mode (EDA H-mode) [Greenwald et al., 1999] are two examples. I-mode is also discovered in AUG [Ryter et al., 2016] and characterized by a steep edge temperature profile while it has a lower gradient of density profile like L-mode. EDA has a pedestal in both temperature and density, but ELMs are replaced by quasi-coherent modes [Greenwald et al., 1999]. EDA was recently realized in AUG [Gil et al., 2020].

1.5 Scope of Thesis

The main goal of this thesis is to investigate heat loads of negative triangularity plasmas and compare them with scaling laws and other scenarios. All the experiments have been conducted at the ASDEX Upgrade tokamak. The result of this study provides the scrape-off layer power width λ_q with different plasma parameters, including poloidal magnetic field strength, toroidal magnetic field direction, and heating power within ASDEX Upgrade negative triangularity shots' parameter range. A further study about λ_q is comparisons with different scenarios, which have similar plasma parameters except for shaping, and comparison with scaling laws.

Chapter 2

Background with Focus on Plasma Shaping and Power Exhaust

2.1 Shaping of Plasma

Fig. 2.1 presents geometry parameters of the plasma, where R is major radius, a is a minor radius, $d^u = R_{geo} - R_{upper}$, and $d^l = R_{geo} - R_{lower}$. R_{upper} and R_{lower} is the most upper and lower point of the separatrix. From these parameters, elongation κ and triangularity δ are defined as follows [Luce, 2013].

$$\kappa = \frac{b}{a} \tag{2.1}$$

$$\begin{aligned} \delta_{upper} &= \frac{R_{geo} - R_{upper}}{a} \\ \delta_{lower} &= \frac{R_{geo} - R_{lower}}{a} \\ \delta &= \frac{\delta_{upper} + \delta_{lower}}{2} \end{aligned} \tag{2.2}$$

In addition, aspect ratio $A = R/a$ and inverse aspect ratio $\epsilon = a/R$ are also defined with presented geometry parameters.

Most of the early tokamak experiments used circular poloidal cross-section because it was a natural choice for making torus shape by bending the cylindrical plasma of linear devices. The first change from a circular cross-section is adding elongation. The elongated shape increases the energy confinement time [ITER Physics Expert Group on Confinement and Transport et al., 1999] and the plasma volume for fixed R and B_{tor}. The second change is adding triangularity. Making a triangle shape makes the top/bottom of the plasma move towards lower R and towards higher B_{tor}. In other words, positive triangularity places the plasma on the high-field side, good curvature. This is beneficial because positioning on a higher toroidal magnetic field stabilizes

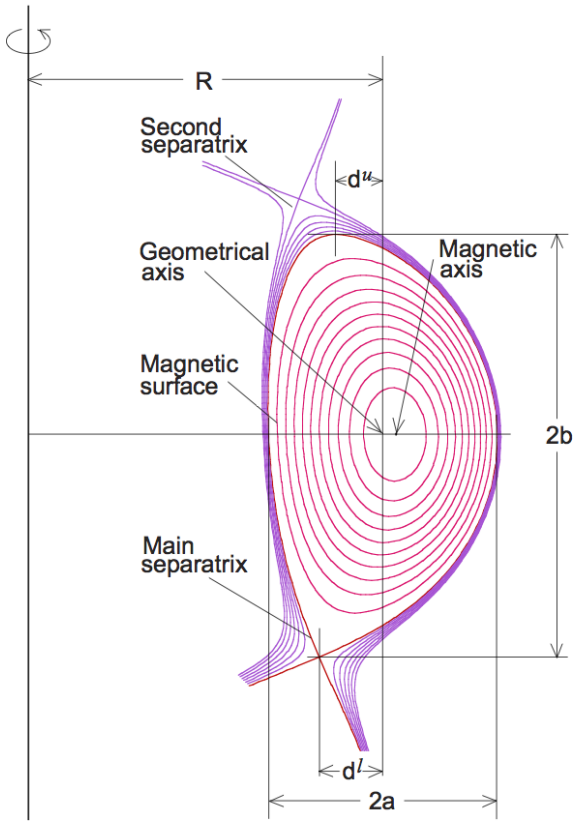

FIGURE 2.1: Sketch of the poloidal cross-section of the tokamak. Geometry parameters of the tokamak are indicated. Retrieved from [fusionwiki, 2014]

against instabilities [ITER Physics Expert Group on Confinement and Transport et al., 1999]. This effect is particularly true for type-I ELMs in standard H-mode operation [Snyder et al., 2002]. With higher elongation and triangularity, these ELMs are more stable, allowing for higher pedestal pressure and overall confinement.

In the meantime, TCV tokamak, which has the flexibility to make various shapes, examined various triangularity of plasma. TCV found an alternative route to high core confinement by inverting the triangularity to negative values [Marinoni et al., 2021b].

2.2 Characteristics of Negative Delta

Stepping away from the paradigm of operating in a type-I ELMy H-mode allowed the exploration of alternative reactor scenarios. One rather radical change is shaping the plasma cross-section such that the upper and lower points are at larger R compared to the axis, in other words having a triangularity with negative values [Fig 2.2].

Although negative triangularity (NT) research, which began in the early

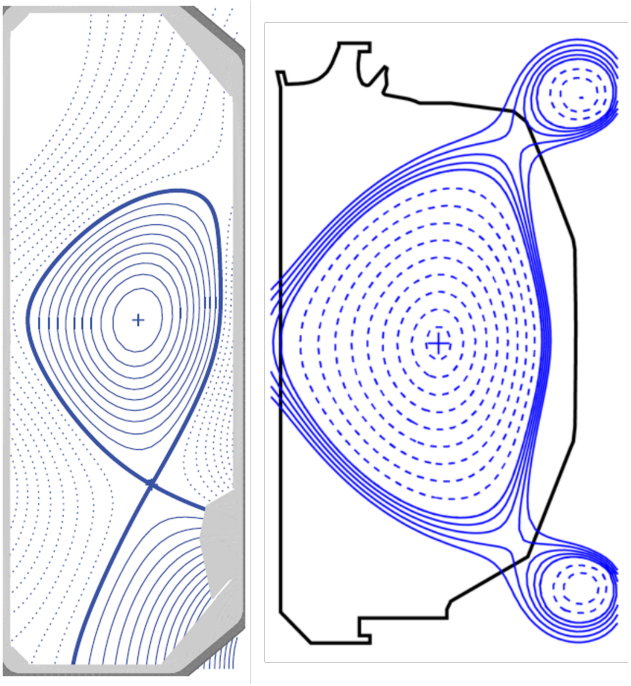

FIGURE 2.2: The poloidal cross-section of negative triangularity shape in TCV and DIII-D. (left) NT shape in TCV tokamak. retrieved from [Coda et al., 2021]. (right) Typical negative triangularity discharge on DIII-D. retrieved from [Marinoni et al., 2018]

1970s and early 1980s, had received little attention, it has gained increasing interest in recent years since the mid-1990s through dedicated experiments on TCV tokamak [Marinoni et al., 2021b]. Ohmically heated L-mode plasmas in a wide range of δ, $-0.41 < \delta < 0.72$, showed improved electron energy confinement time as δ is more negative [Pochelon et al., 1999, Moret et al., 1997]. Fig. 2.3 shows that NT has improved confinement time than $\delta > 0$ with early and recent results about τ_e and H_{98y2}, for definition see [ITER Physics Expert Group on Confinement and Transport et al., 1999], respectively. This enhanced energy confinement is explained by a reduction of turbulent transport [Marinoni et al., 2009]. The reduction of turbulence in the outer core region of the plasma is the main advantage, increasing the pressure in the region relevant to the fusion process. This allows to recover the same core pressure, even if no pedestal is present, and hence allows the operation with an L-mode edge. Staying in L-mode has the advantage of avoiding the steep pedestal gradients and, with this, the ELMs. Further, without the need to stay in H-mode, NT might be able to radiate more power in the confined region, reducing the power exhaust challenge significantly.

Especially a reliable assessment of the power fall-off length, one of the main parameters for heat exhaust, is yet to be conducted. First experimental results are reported for TCV L-mode, showing a more narrow fall-off length in negative triangularity [Faitsch et al., 2018], and from DIII-D, showing that negative

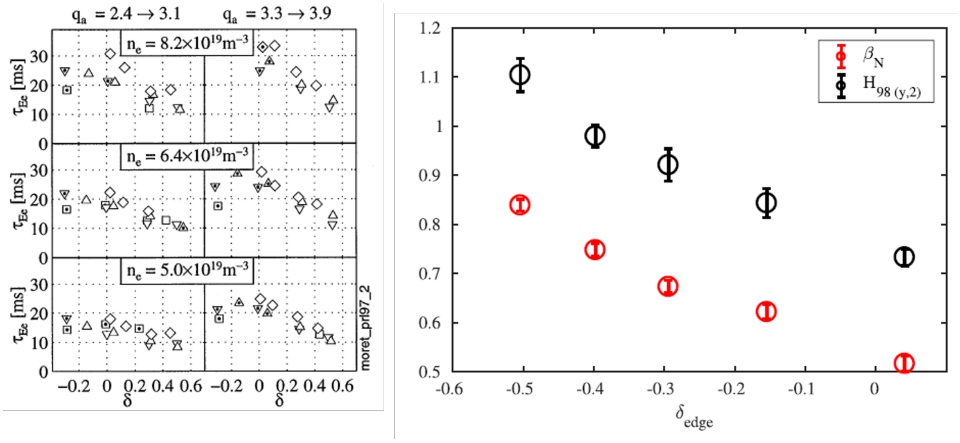

FIGURE 2.3: Confinement time versus δ in TCV negative triangularity experiments. (left) Shape dependence of the electron energy confinement time for various δ. Retrieved from [Moret et al., 1997]. (right) the H-mode confinement enhancement factor (H_{98y2}) over a triangularity scan. Retrieved from [Coda et al., 2021]

triangularity L-mode has a broader fall-off length than in H-mode [Marinoni et al., 2021a].

2.3 Influence of Magnetic Field Direction

Not only the choice of the plasma scenario can have an important impact on the tokamak operation. An important choice for the operation is the direction of the toroidal magnetic field. In ASDEX Upgrade lower single null discharges, the helicity is determined by the divertor structure. Since the divertor target tiles are toroidally inclined to avoid leading edges, two combinations of toroidal and poloidal magnetic field direction can be realized. Thus, in AUG, one configuration is B_{tor} is negative (toward), and I_p is positive. The other is that B_{tor} is positive (reversed), and I_p is negative. These two configurations have different directions of vertical drift v_d because the vertical drift direction of electrons and ions depends on the sign as described below. The best-reported impact of changing configurations is the impact on the power needed to transition from L- to H-mode [Wagner et al., 1985].

2.3.1 Vertical Drift of Moving Center

Because the toroidal magnetic field in the tokamak is proportional to $1/R$, there is naturally a gradient of the magnetic field ∇B inside the tokamak. The charged particles have a cyclotron motion along the magnetic field, and their center of gyro motion is drifting due to ∇B with velocity.

$$\mathbf{v_d^{\nabla B}} = -\frac{W_\perp}{q}\frac{\nabla B \times \mathbf{B}}{B^3} \tag{2.3}$$

Eq. 2.3 is ∇B-drift where $W_\perp = 1/2mv_\perp^2$ is the kinetic energy of perpendicular to the magnetic field. In addition, the curvature of the magnetic field leads to a drift velocity of:

$$\mathbf{v_d^k} = -\frac{2W_\parallel}{qR_k^2}\frac{\mathbf{R_k}\times\mathbf{B}}{B^2} \tag{2.4}$$

Where $W_\parallel = 1/2mv_\parallel^2$ is the kinetic energy of parallel to the magnetic field and R_k is the radius of curvature. Eq. 2.4 is called curvature drift. These two magnetic field-related drifts are often combined using $\nabla|B|/|B| = -\mathbf{R_k}/R_k^2$.

$$\mathbf{v_d^{\nabla B+k}} = \mathbf{v_d^{\nabla B}} + \mathbf{v_d^k} = -(W_\perp + 2W_\parallel)\frac{\nabla B\times\mathbf{B}}{qB^3} \tag{2.5}$$

Due to the q dependency in Eq. 2.5, ions and electrons are drifting in opposite directions. This charge separation generates an electric field E.leading to an $\mathbf{E}\times\mathbf{B}$ drift velocity.

$$\mathbf{v_d^{E\times B}} = \frac{\mathbf{E}\times\mathbf{B}}{B^2} \tag{2.6}$$

In the case of Eq. 2.6, there is no charge dependence, unlike the vertical drift, Eq 2.5 other drifts. These three drifts come from the kinetic model of the plasma, deriving an equation of motion of the guiding center [Stroth, 2018]. Due to the stronger toroidal field compared to poloidal, $B_{tor} \gg B_{pol}$, the ∇B and curvature drifts lead to a vertical drift motion. The $\mathbf{E}\times\mathbf{B}$ drift leads to a radial outwards movement of the plasma.

2.3.2 L-H Transition

After the discovery of the H-mode, it was observed that the toroidal magnetic field direction has an important influence on the power threshold for the transition from L- to H-mode [Wagner et al., 1985]. Due to the fact that H-mode is the preferred operational regime, the direction with a lower threshold power is 'favorable' and routinely used in tokamaks all over the world as a 'normal' operational direction. This favorable direction is achieved when the ion $v_d^{\nabla B}$ direction is pointing towards the X-point. In AUG, the favorable direction is for a standard lower single null plasma configuration with a negative toroidal magnetic field. Conversely, the unfavorable direction is also called the 'reversed' direction, having the ion $v_d^{\nabla B}$ pointing away from X-point. The reversed direction is not favorable for H-mode, so it is named unfavorable configuration. It is important to note here that while the naming of favorable and unfavorable is still kept, it is not to be taken as an adverse effect if not operating in H-mode. In the case of the I-mode and NT L-mode, the transition to H-mode is to be avoided. Thus, it can be beneficial to operate with 'reversed' or 'unfavorable' drift direction.

2.4 Scrape-Off Layer Heat Flux

In a fusion reactor, all the externally applied and generated fusion energy is balanced by the lost energy in steady-state conditions. The plasma-facing materials will receive the lost energy, and in the case of the energy of charged particles, this will be handled mostly at the divertor. However, the divertor can withstand a specific power limit, depending on the material and cooling used. Thus, studying the power exhaust is getting important to control and predict the power onto the divertor tiles. The most representative parameter in the power exhaust studying is the power fall-off length. After obtaining the fall-off length, the peak heat load onto the divertor can be estimated. In order to reduce the peak value below the material limit, impurity seeding is used. The amount of seeding is determined by the power fall-off length and the reduction needed.

2.4.1 Power Balance

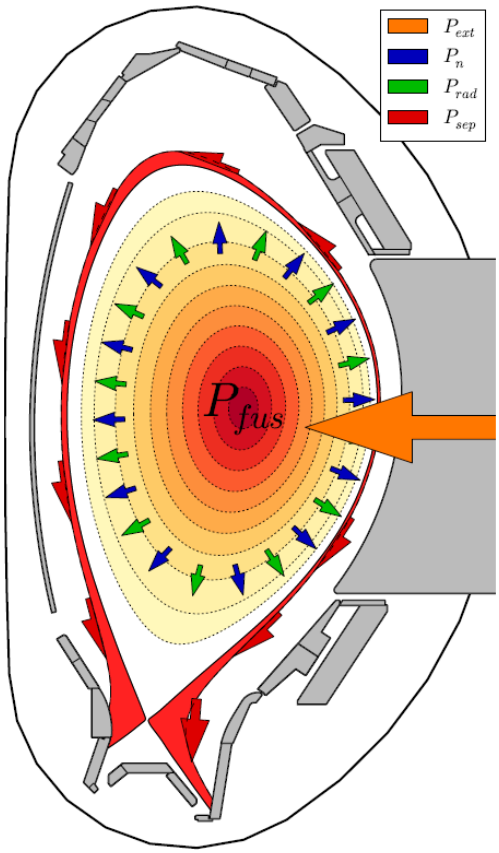

FIGURE 2.4: Sketch of the power fluxes in the fusion reactor. Retrieved from [Sieglin, 2014]

Fig. 2.4 shows a poloidal cross-section of ASDEX Upgrade. The color cod-

ing in the confined region indicates the pressure gradient. The arrows indicate different contributions to the power balance:

$$P_{ext} + P_{fusion} = P_n + P_{rad} + P_{sep} \tag{2.7}$$

Where $P_{fusion} = P_\alpha + P_n$ from D-T reaction, not relevant for most present-day tokamaks but dominates in future fusion power plants. Most of the fusion power is carried by neutrons, blue arrows, not being confined by magnetic fields and leaving the plasma uniformly on all first wall components. External heating power P_{ext}, orange arrow, is applied to increase the temperature of the plasma. The energy of the confined plasma is lost by radiation from the confined region P_{rad}, green arrows, and by power crossing the separatrix by charged particles P_{sep}, red arrows. Here we concentrate on the power following the open field lines towards the divertor target. Thus, P_{sep} can be described as follows.

$$P_{sep} = P_{ext} + P_\alpha - P_{rad} \tag{2.8}$$

In the case of the ITER like device, expected P_{ext} is 50 MW, P_α is 100 MW, and P_{rad} is around 30 MW. This is above realizable machine limits. Without further reduction, this would lead to an unacceptable power load of 120 MW onto the divertor structure. Not only the peak heat flux would be intolerable, but also the total amount of power can not be handled by the cooling capability of the ITER divertor, estimated to receive less than 10 MW. Therefore, a large part of P_{sep} needs to be exhausted before reaching the divertor. This is achieved by introducing impurities that can efficiently radiate the majority of this power. For ITER, it is foreseen to operate in a regime called (partial) detachment. With the detachment, the heat load is reduced, and the pressure along field lines is reduced. This is needed to reach low electron temperature at the target as well as reduce the particle flux, and both are needed to reduce erosion. These impurities radiate in the SOL, reducing the power onto the divertor P_{div}:

$$P_{div} = P_{ext} + P_\alpha - P_{rad}^{core} - P_{rad}^{SOL} \tag{2.9}$$

2.4.2 Scrape-Off Layer Heat Flux

The steady-state heat flux impinging the divertor target in attached conditions is characterized by a model introduced by [Eich et al., 2011]. The SOL heat flux can be described by an exponential decay starting from the separatrix [Wagner et al., 1985]:

$$q_{exp}(s) = q_0 \exp\left(-\frac{s}{\lambda_q f_x}\right) \quad [\mathrm{MW/m^2}] \tag{2.10}$$

where q_0 is the peak heat flux at the separatrix, s is the position from the separatrix, λ_q is the upstream power fall-off length, and f_x is the poloidal flux expansion which will be covered in a later section. q_{exp} at $s < 0$ is not considered because inside of separatrix means inside of closed field line. A universal quantity is defined as the integral power fall-off length λ_{int}, which

can be used to derive the peak heat flux onto the divertor target q_{max} [Loarte et al., 1999].

$$\lambda_{int} = \frac{\int q(s)ds}{q_{max}} \quad [\mathrm{mm}] \tag{2.11}$$

$$q_{max} = \frac{P_{div}}{2\pi R_{div}\lambda_{int} f_x} \quad [\mathrm{MW/m^2}] \tag{2.12}$$

Where P_{div} is power arrived at the divertor and R_{div} is the radius from the tokamak axis to the divertor. Eq. 2.10 is not for the divertor heat measurement. Below the X-point, heat is able to spread by perpendicular transport and reduce the peak heat flux by increasing the area. Assuming diffusive transport and in the limit of 1D, it can be described by a Gaussian [Eich et al., 2011]:

$$g(s) = \frac{1}{S f_x \sqrt{\pi}} \exp\left(-\left(\frac{s}{S f_x}\right)^2\right) \tag{2.13}$$

where S is divertor broadening. In order to get the divertor heat flux profile, Eq. 2.10 and Eq. 2.13 are convoluted as follows [Eich et al., 2011].

$$q(s) = \frac{q_0}{2} \exp\left(\left(\frac{S}{2\lambda_q}\right)^2 - \frac{s}{\lambda_q f_x}\right) erfc\left(\frac{S}{2\lambda_q} - \frac{s}{\lambda_q f_x}\right) \quad [\mathrm{MW/m^2}] \tag{2.14}$$

With Eq. 2.14, a 1D heat flux profile on the divertor can be obtained. Due to the axis-symmetry of the tokamak, this 1D profile is describing the full heat flux profile. In addition, the parameters of this 1D function are linked to λ_{int}, and the integral power fall-off length has a good approximation for the profile by Eq. 2.14 [Makowski et al., 2012].

$$\lambda_{int} \approx \lambda_q + 1.64S \quad [\mathrm{mm}] \tag{2.15}$$

In the case of a purely exponential decaying profile, without divertor broadening, Eq. 2.10 follows relation 2.16 with $\lambda_q = \lambda_{int}$

$$\int_0^\infty q(s)ds = q_0 \lambda_q f_x \tag{2.16}$$

All together with these equations, from λ_q, the peak heat flux on the divertor is estimated.

$$q_{max} = \frac{P_{div}}{2\pi R_{div}(\lambda_q + 1.64S) f_x} \quad [\mathrm{MW/m^2}] \tag{2.17}$$

$$q_{max} = q_0 \frac{\lambda_q}{\lambda_q + 1.64S} \quad [\mathrm{MW/m^2}] \tag{2.18}$$

Eq. 2.18 is presenting that q_{max} can be lower with the lager S [Fig. 2.5], where λ_{target} fall-off length on divertor target and S_{target} broadening on divertor target. Moreover, λ_q and S approximate λ_{int}, and from λ_{int}, q_{max} can be estimated.

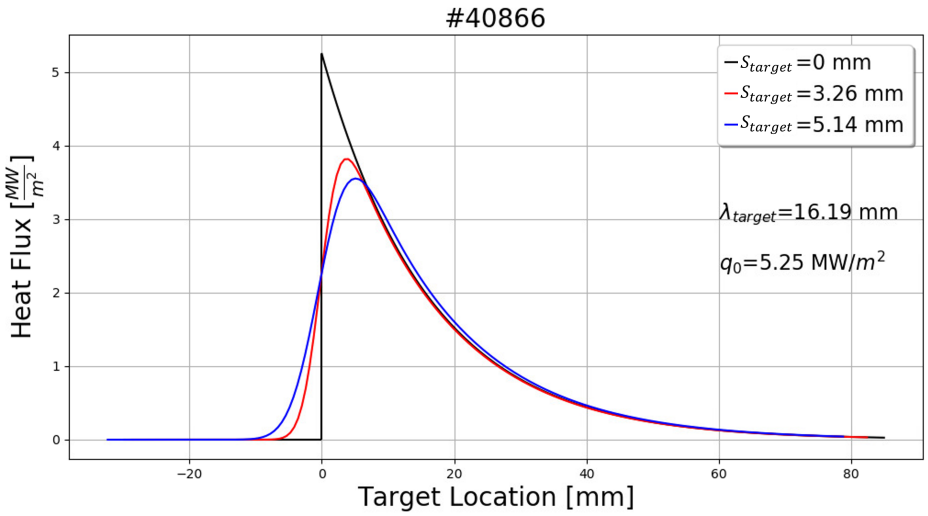

FIGURE 2.5: Effect of broadening on q_{max}

2.4.3 Flux Expansion

In Eq. 2.14, the heat flux profile's width depends on flux expansion f_x. The flux expansion is an important factor that increases the area over which power is distributed. The flux expansion can be divided into two contributions, the magnetic contribution as well as a contribution by the poloidal angle between field lines and the divertor [Fig. 2.6].

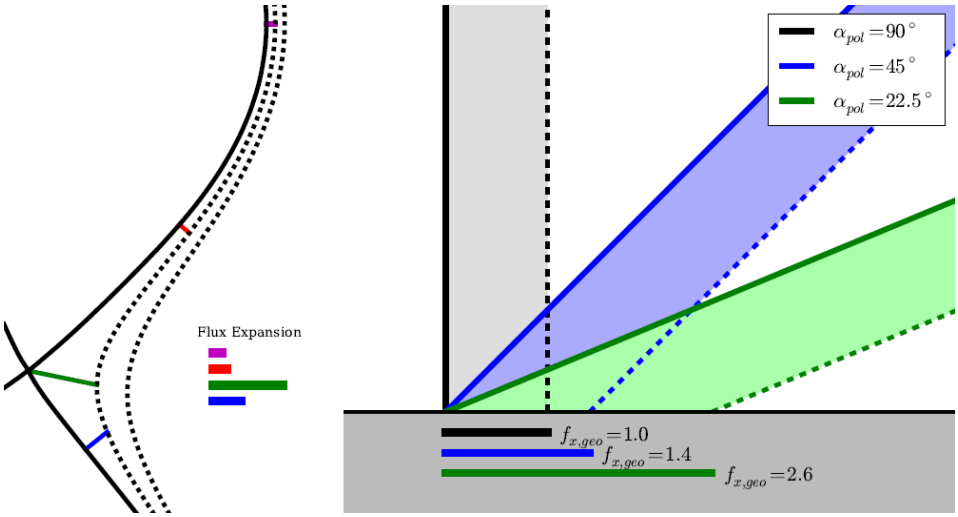

FIGURE 2.6: Illustration of magnetic flux expansion (left) and flux expansion by geometry (right). retrieved from [Sieglin, 2014]

$$f_{x,mag} = \frac{R_{MP} B_{pol}^{MP}}{R_{div} B_{pol}^{div}} \tag{2.19}$$

Where MP stands for outer midplane, div is the divertor, R is the major radius of the MP and divertor, and B_{pol} is poloidal magnetic field strength. Eq. 2.19 is the magnetic contribution to the flux expansion. It can be seen from Fig. 2.6 (left) and Eq. 2.19 that the magnetic flux expansion gets more extensive as it gets closer to the X-point because B_{pol} near the X-point is weak. The second contribution is called the geometric flux expansion and is calculated as Eq. 2.20 with poloidal projection angle of magnetic field line onto divertor α_{pol}.

$$f_{x,geo} = \frac{1}{\sin \alpha_{pol}} \tag{2.20}$$

The geometric flux expansion increases as the divertor is more inclined with respect to the flux and decreases as α_{pol} is closer to the vertical [Fig. 2.6]. Thus, the total flux expansion considering both can be written as the product of magnetic and geometric flux expansion.

$$f_x = f_{x,mag} \cdot f_{x,geo} = \frac{R_{MP} B_{pol}^{MP}}{R_{div} B_{pol}^{div}} \cdot \frac{1}{\sin \alpha_{pol}} \tag{2.21}$$

According to Eq. 2.17, it is advantageous to increase f_x to decrease q_{max} with respect to power flux. For this, a reactor design makes the divertor inclined to maximize f_x with larger α_{pol}. However, the field line angle and the flux expansion have to be kept above a threshold with allowing construction tolerances.

2.5 Infrared Thermography

The main target of this thesis is to study the heat flux of NT. Before getting heat flux onto the divertor tile, the temperature evolution calculation must first be done and is essential. The temperature is measured by an infrared (IR) measurement without direct contact, detecting the thermal radiation of a heated object. IR thermography is used on ASDEX Upgrade and measures emitted photon flux from the divertor for a given temperature according to Planck's law. After the temperature information is obtained, heat flux q can be calculated.

2.5.1 Temperature

In the case of an idealized black body, an object absorbs electromagnetic radiation at all wavelengths. Planck's law [Planck, 1900a, Planck, 1900b] describes the spectral radiance $M_\lambda^0(\lambda, T)$ per area dA and wavelength interval $d\lambda$ for the absolute temperature T of a black body.

$$M_\lambda^0(\lambda, T) dA d\lambda = \frac{2\pi h c^2}{\lambda^5} \frac{1}{e^{\frac{hc}{\lambda k_B T}} - 1} dA d\lambda \quad [\mathrm{W/m^3}] \tag{2.22}$$

Where k_B is the Boltzman constant, h is the Plank constant, and c is the speed of light in a vacuum. However, the plasma-facing components are not

ideal blackbodies. For AUG, divertor tiles consist of full tungsten tiles and tungsten-coated carbon tiles. Thus, to take into account materials' properties, emissivity ϵ, which is the ratio between the surface emission and that of the ideal blackbody, has to be considered.

$$I^0_\lambda(\lambda, T)dAd\lambda = \epsilon(\lambda, T)\frac{2\pi hc^2}{\lambda^5}\frac{1}{e^{\frac{hc}{\lambda k_B T}} - 1}dAd\lambda \quad [\mathrm{W/m^3}] \tag{2.23}$$

$I^0_\lambda(\lambda, T)$ is the emission of a surface, and emissivity is a function of temperature and wavelength. This Plank's law is again modified because the IR camera used at AUG experiments counts photons. To change LHS to photon flux, it is divided by photon energy $E_\gamma = hc/\lambda$.

$$\Gamma^0_\lambda(\lambda, T)dAd\lambda = \epsilon(\lambda, T)\frac{2\pi c}{\lambda^4}\frac{1}{e^{\frac{hc}{\lambda k_B T}} - 1}dAd\lambda \quad [\mathrm{s^{-1}m^{-3}}] \tag{2.24}$$

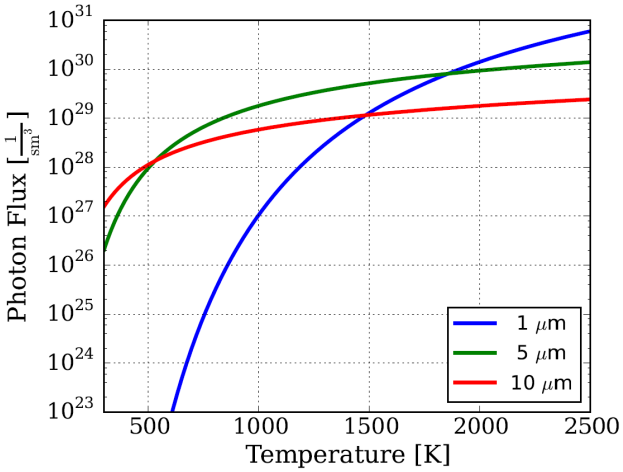

FIGURE 2.7: Photon flux for a black body depends on the temperature of different photon wavelengths. retrieved from [Faitsch, 2017]

Fig. 2.7 shows emitted photon flux depending on temperature for three wavelength values. For the envisaged temperature range of the AUG divertor tiles of room temperature up to 2500 K, a system at 5 µm is best suited. In AUG, around 4.7 µm wavelength is picked because an emissivity of 4.7 µm for the divertor surfaces temperature during the operation shows the highest photon flux sensitivity, considering the specifications of the IR camera.

2.5.2 IR Camera

An IR thermography camera system is used in ASDEX Upgrade in order to study the divertor heat flux [Sieglin et al., 2015]. The IR camera for a fusion reactor requires magnetic and electric shielding to withstand a high magnetic field during the operation. Fig. 2.8 illustrates the detector in the camera hous-

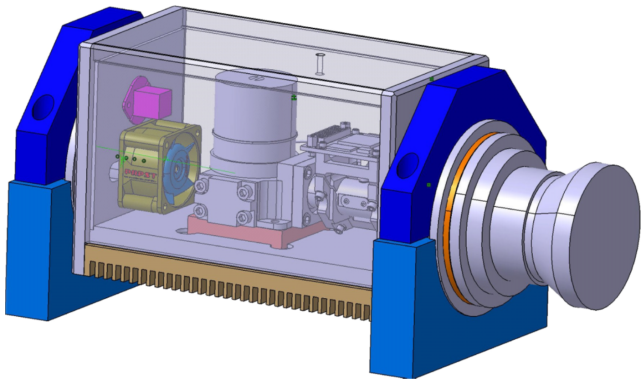

FIGURE 2.8: Illustration of the detector. The camera housing is shown as transparent. retrieved from [Sieglin et al., 2015]

ing used for this thesis. The IR detector used for the IR system is a digital 640 × 512 pixels, PelicanD 640 detector from SCD. The IR detector has a spectral response from $\lambda = 3.6\,\mu m$ to $4.9\,\mu m$ limited by spectral filters. In the full frame mode, a frame rate is 300 Hz (3.33 µm). For the smallest subwindow, the frame rate can be raised up to 5.5 kHz (0.18 µm) with 320 × 4 pixels. the change of frame modes and manipulating camera parameters can be done by LabVIEW with the National Instrument hardware as well as data acquisition [Sieglin et al., 2015]. Fig. 2.9 shows IR camera locations, targets,

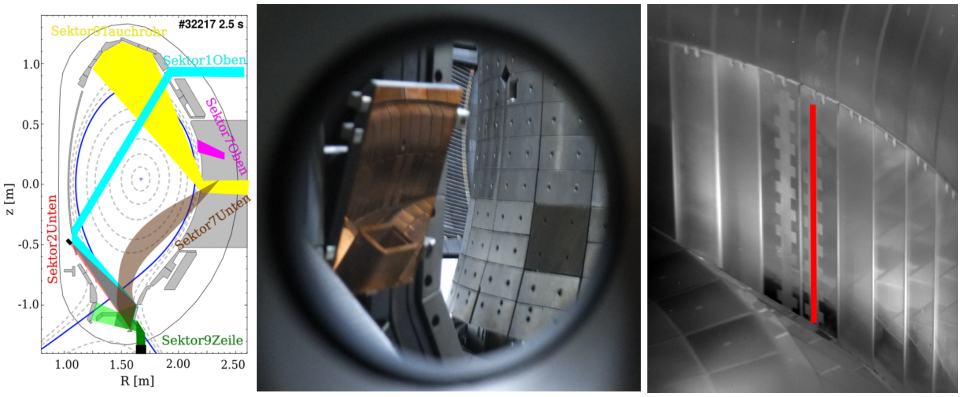

FIGURE 2.9: (left) IR cameras located in AUG. (middle) port for IR camera at sector 7 of AUG. (right) Sektor7Unten IR camera's full frame view and outer divertor tile1 (lower outer divertor). The red line is a sample line for 1D profile calculation. (left) (middle) are retrieved from [AUG webpage, 2022], (right) is from [Sieglin et al., 2016]

and the full frame view. For the Sektor7Unten IR camera, which is only used in this thesis, a mirror is used for observing the outer divertor. This camera is routinely used to observe the lower outer divertor, tile 1. In this thesis, the camera view was slightly shifted to be able to also observe the curved tile 2 vertically above tile 1. Tile 1 is marked with a red line in Fig. 2.9 (right).

2.5.3 Heat Flux

With the IR camera system and Equation 2.24, the surface temperature evolution $T(s,t)$ can be obtained. The quantity s denotes the position on the surface of the divertor tile, and t represents the time within the measurement. With this T, the heat flux density can be calculated using the heat flux Fourier's law with the heat conductivity κ and the gradient of temperature ∇T.

$$q = -\kappa \nabla T \quad [\mathrm{W/m^2}] \tag{2.25}$$

In order to solve Eq. 2.25, the temperature distribution inside the divertor tile has to be known. This is calculated from the heat diffusion equation.

$$\rho c_p \frac{\partial T}{\partial t} = \nabla(\kappa \nabla T) \tag{2.26}$$

Where T is the temperature on the tile's surface, t is the time, ρ is the density of the material, and c_p is the specific heat capacity of the divertor tile's material. In order to solve this non-linear differential equation, substitution and numerical method are performed by a code called THEODOR (**TH**ermal **E**nergy **O**nto **D**ivert**OR**) [Herrmann et al., 1995, Sieglin et al., 2015, Nille et al., 2018]. The heat conductivity depends on the material temperature, so it is necessary to solve the whole Eq. 2.26. This dilemma can be solved by introducing heat flux potential U.

$$U(T) = \int_0^T \kappa(T')dT' \quad [\mathrm{W/m}] \tag{2.27}$$

In addition, heat conductivity κ easily shows the following relation from the heat potential.

$$\frac{\partial U(T)}{\partial T} = \kappa(T) \quad [\mathrm{W/Km}] \tag{2.28}$$

By using the partial derivatives Eq. 2.29 and Eq. 2.28, Eq. 2.26 can be rewritten.

$$\begin{aligned} \frac{\partial U}{\partial t} &= \frac{\partial U}{\partial T}\frac{\partial T}{\partial t} = \kappa(T)\frac{\partial T}{\partial t} \\ \frac{\partial U}{\partial x} &= \frac{\partial U}{\partial T}\frac{\partial T}{\partial x} = \kappa(T)\frac{\partial T}{\partial x} \\ \frac{\partial^2 U}{\partial x^2} &= \frac{\partial}{\partial x}\left(\kappa(T)\frac{\partial T}{\partial x}\right) = \nabla(\kappa \nabla T) \end{aligned} \tag{2.29}$$

$$\begin{aligned} \rho c_p \left(\frac{1}{\kappa}\frac{\partial U}{\partial t}\right) &= \nabla(\kappa \nabla T) \\ \rho c_p \left(\frac{1}{\kappa}\frac{\partial U}{\partial t}\right) &= \frac{\partial^2 U}{\partial x^2} \\ \frac{\partial U}{\partial t} &= D\frac{\partial^2 U}{\partial x^2} \end{aligned} \tag{2.30}$$

With this simplified linear differential diffusion equation, where $D = \kappa/\rho c_p$, heat flux potential can be obtained. Finally, and finally, heat flux can be calculated numerically by the following equation.

$$\begin{aligned} q &= -\kappa \nabla T \\ &= -\nabla U \\ &\approx \frac{3U(x) - 4U(x+\delta x) + U(x+2\delta x)}{2\delta x} \end{aligned} \tag{2.31}$$

Eq. 2.31 where δx is the resolution of the grid of the IR camera. Obtained q from Eq. 2.31, the profile can be fitted by Eq. 2.14. As a result of fitting, power fall-off length on target $\lambda_{q,target}$, broadening on target S_{target}, the peak of profile q_{max}, and integrated fitted profile P_{div} are acquired. With flux expansion f_x from Eq. 2.21, fall off length $\lambda_q = \lambda_{q,target}/f_x$ and broadening $S = S_{target}/f_x$ can be calculated.

2.6 Scaling Laws and Heuristic Model

Predictions for heat flux fall-off length currently exist in two axes. One is the heuristic model derived from theory, the Goldston model, and the other is an empirical regression from actual measurement data. Three empirical regressions are used in this thesis to compare with the measured data. The H-mode model is made of AUG and JET data, the L-mode model is made of AUG data, and the multi-machine H-mode will be introduced.

2.6.1 Regression Scaling Laws

$$\lambda_q^{\mathrm{H-mode,Mulit}} = 0.63 \pm 0.08 [B_{pol,MP}^{-1.19\pm0.08}\,(\mathrm{T})] \tag{2.32}$$

Eq. 2.32 is H-mode regression model made by data from various fusion devices [Eich et al., 2013], where $B_{pol,MP}$ is the poloidal magnetic field at the outer midplane. In this multi-machine study, it was possible to scale λ_q with a single parameter, showing the strong influence of B_{pol} on λ_q. Figure 2.10 shows the dependence of B_{pol}, which showed the strongest dependence on λ_q, as mentioned earlier. These regression models make it possible to predict the fall-off length of future machines by extrapolating from the existing devices. As a result, predicting the case of ITER, $R = 6.2\,m$, $a = 2.0\,\mathrm{m}$, $\kappa = 1.7$, $P_{SOL} = 120\,\mathrm{MW}$, $B_{tor} = 5.3\,\mathrm{T}$, $I_P = 15\,\mathrm{MA}$, $q_{cyl} = 2.42$, a fall-off length of about 1 mm is expected [Eich et al., 2013].
Among the plasma parameters in the fusion device, some values can be predetermined before discharge. These are called engineering parameters, and through these values, the λ_q was regressed using power law $\lambda_q = C \cdot X^x Y^y Z^z$.

$$\lambda_q^{\mathrm{H-mode,Eich}} = 0.73 \pm 0.38 [B_{tor}^{-0.78\pm0.25}\,(\mathrm{T})] q_{cyl}^{1.2\pm0.27} [P_{SOL}^{0.1\pm0.11}\,(\mathrm{MW})] R_{geo}^{0.02\pm0.2} \tag{2.33}$$

$$\lambda_q^{\mathrm{L-mode,Sieglin}} = 1.45 \pm 0.13 [B_{tor}^{-0.78\pm0.25}\,(\mathrm{T})] q_{cyl}^{1.07\pm0.07} [P_{SOL}^{-0.14\pm0.05}\,(\mathrm{MW})] \tag{2.34}$$

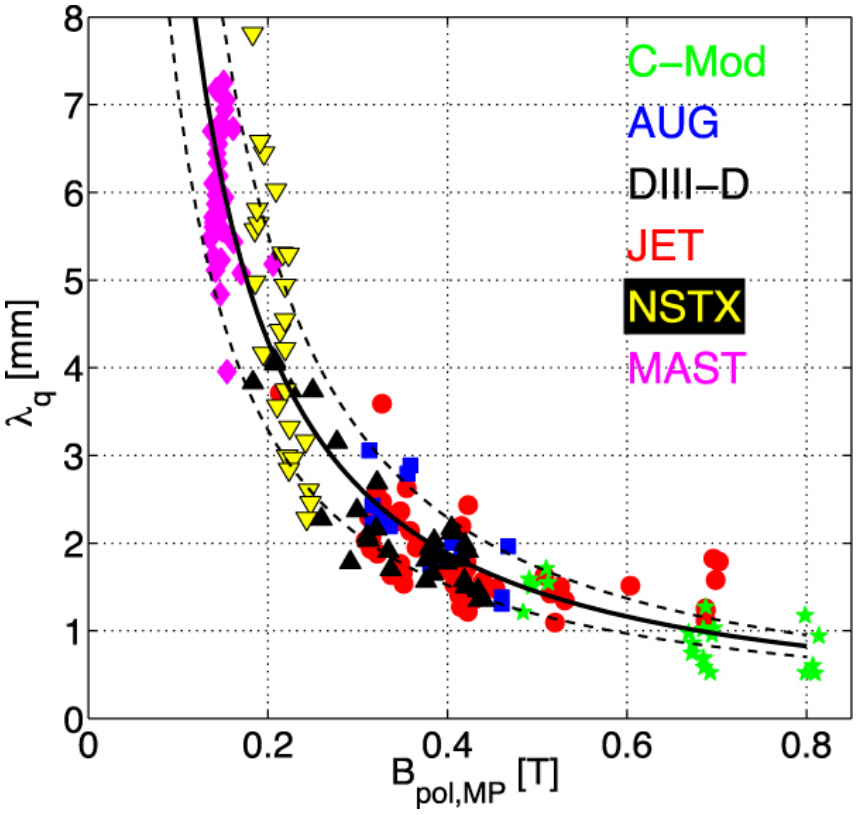

FIGURE 2.10: Poloidal magnetic field at the outer midplane versus power fall-off length. The solid line and dashed lines are regression model and errors, respectively. Retrieved from [Eich et al., 2013]]

These two equations are regression models including AUG data for H-mode Eq. 2.33 [Eich et al., 2011] and L-mode Eq. 2.34 [Sieglin et al., 2016], respectively. where B_{tor} is toroidal magnetic field strength, q_{cyl} is cylindrical safety factor, P_{SOL} is power crossing separatrix, and R_{geo} is major radius. The safety factor is used because connection length $L_c = 2\pi Rq$ is the important parameter for SOL transport, and it is proportional to the safety factor. q_{cyl} is used instead of q because q has ∞ at X-point (q_{100}).

$$\begin{aligned} q &= \frac{a}{R}\frac{B_{tor}}{B_{pol}} \\ q_{cyl} &= \frac{2\pi a \epsilon B_{tor}}{\mu_0 I_P}\frac{(1+\kappa^2)}{2} \end{aligned} \tag{2.35}$$

In the case of the B_{pol}, which already showed a great influence on λ_q, it is excluded as a single parameter for the regression model because the safety factor q contains B_{pol}. This consideration of B_{pol} in q makes the negative multiplier on B_{tor} because the impact on λ_q of both magnetic fields is different. P_{SOL} can also be decided before discharge, and the influence of power is checked in Section. 2.4.2.

2.6.2 Heuristic Drift-Based Model

So far, in this section, there have been only empirical scaling laws based on experimental data. However, there is also a heuristic model developed from a theoretical background [Goldston, 2012]. Fig. 2.11 shows scrape-off layer width

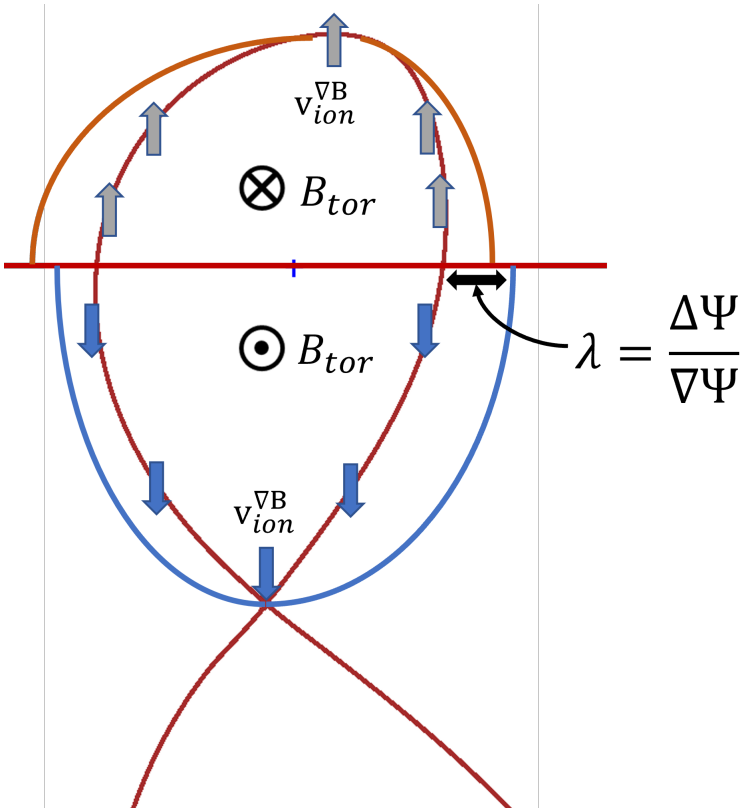

FIGURE 2.11: Sketch about gyro center movement and drift direction for each toroidal magnetic field direction.

changing with different toroidal magnetic fields and ion ∇B drifts. The blue and grey arrows indicate vertical drift [Section. 2.3.1].The blue and orange solid lines are schematics of the gyro center movement of ions in a poloidal cross-section. This heuristic model interpreted the scrape-off layer width as the influence of particle drifts. Vertical drifts carry the particles across the separatrix onto open field lines and are balanced with the parallel flow. Using this interpretation, the SOL width is understood as radial displacement by vertical drifts. The poloidal width λ is defined as Eq. 2.36

$$\lambda = \frac{\Delta\Psi_p}{|\nabla\Psi_p|} \tag{2.36}$$

Where Ψ is poloidal flux, $\Delta\Psi_p$ is the displacement in flux, and $|\nabla\Psi_p|$ is the gradient of the flux to translate into real space coordinates (m). This poloidal width λ is associated with the width of the power carrying layer, the power

fall-off length λ_q.

$$\langle v_D \rangle = \frac{2T}{eZRB}\hat{z} \tag{2.37}$$

The model balances the drift velocity with the parallel velocity of particles in the SOL. Eq. 2.37 is the Maxwellian averaged ∇B and curvature drift velocity, where T is temperature, e is a single electron charge, Z is the average ion charge, R is the major radius, B is magnetic field strength, and $\hat{z}$ is a unit vector in the vertical direction. The displacement in poloidal flux along the path from the MP to the lowest point S_x is expressed as:

$$\Delta\Psi_p = \frac{1}{v_\parallel}\int_{MP}^{S_x}(\langle v_D \rangle \cdot \nabla\Psi_p)dl_\parallel \tag{2.38}$$

where $v_\parallel$ averaged parallel velocity which is assumed as $v_\parallel \approx 0.5c_s$ with ion speed sound c_s. To derive λ and to integrate Eq. 2.38, the definition of the poloidal magnetic field B_P is used.

$$B_P = \frac{|\nabla\Psi_p|}{R} \tag{2.39}$$

Using Eq. 2.39 and Eq. 2.38, the poloidal width can be expressed as follows.

$$\lambda = \frac{2Ta}{v_\parallel eZB_P R} \tag{2.40}$$

using here the formula as in [Faitsch et al., 2015] with the explicit delta dependence.

$$\lambda = \frac{2T}{v_\parallel eZB_P R}a \cdot (1 + \delta_x) \tag{2.41}$$

Where the + sign in front of δ_x corresponds to the outer divertor, and x in δ_x is upper or lower, depending on the drift direction, δ_{upper} for the unfavorable and δ_{lower} for the favorable regime. This Eq. 2.40 is modified again to match with empirical scaling laws with the following relations [Goldston, 2012, Eich et al., 2011].

$$\begin{aligned} v_\parallel \approx 0.5c_s &= \frac{1}{2}\left(\frac{(1+Z)T}{Am_p}\right)^{\frac{1}{2}} \\ P_{SOL} &= \frac{4\pi R\lambda B_P \chi_{0,S} T^{7/2}}{(7/4)BL_\parallel} \\ T^{\frac{1}{2}} &= \left(\frac{P_{SOL}(7/4)BL_\parallel}{4\pi R\lambda B_P \chi_{0,S}})\right)^{\frac{1}{7}} \end{aligned} \tag{2.42}$$

Where A is the average ion mass, m_p is proton mass, χ is Spitzer-Härm electron thermal conductivity and L is connection length. The values for A, Z, effective atom number Z_{eff}, κ, and ϵ are replaced with actual numbers in experiments from JET and AUG [Eich et al., 2011]. As a result, the drift-based heuristic model can be expressed like the empirical model.

$$\lambda_q^{\text{HeuristicDriftmodel}} = 0.93[B_T^{-0.875}(T)]q_{cyl}^{1.125}[P_{SOL}^{0.125}(MW)](1 \pm \delta_x)^{0.875} \tag{2.43}$$

Chapter 3

ASDEX Upgrade Data Acquisition

This chapter explains how to achieve and what the data is used in later results and analysis. Before examining the heat flux data, other plasma parameters must also be included in the data set for studying power exhaust. Hence, this chapter introduces the used plasma parameters, and how these values are obtained. Further, it explains how heat flux data from the IR measurements are processed.

3.1 Plasma Parameters Obtained by Equilibrium Reconstruction

At ASDEX-Upgrade, the main codes for equilibrium are the FPP used in the control system, cliste (EQI, EQH) [Schneider et al., 2000], and IDE [Fischer et al., 2016]. IDE has the highest fidelity for the NT scenario and was chosen accordingly.

3.1.1 Used Plasma Parameters

First of all, the flux expansion f_x is selected for heat flux calculation Eq. 2.14. Radius from tokamak axis to the divertor R_{div} and total heating power $P_{tot} = P_{ohmic} + P_{NBI} + P_{ECR} + P_{ICR}$, where P_{ohmic} ohmic heat, P_{NBI} neutral beam injection heating, P_{ECR} electron cyclotron resonance heating, P_{ICR} ion cyclotron resonance heating, are used for getting q_{max} relation to λ_q [Eq. 2.17]. In order to calculate fall-off length models [Section. 2.6], toroidal magnetic field B_t, core radiation $P_{rad,core}$, triangularity δ, and parameters for q_{cyl}, major radius R_{geo}, minor radius a_{geo}, poloidal magnetic field at the midplane $B_{p,MP}$, and elongation κ, are gained from equilibrium code. Last but not least, to check a correlation between λ_q and plasma parameters, stored energy W_{mhd}, the temperature of electron T_e from IDA [Fischer et al., 2010], the density of electron n_e from the interferometer, confinement time H_{98y2}, safety factor q_{95}, and nor-

malized pressure β are acquired and used. However, except P_{tot}, W_{mhd}, and H_{98y2}, there was no exhibiting correlation. Thus, in this thesis, P_{tot} is used as the main parameter for heat flux study, and W_{mhd} and H_{98y2} are not handled because they are connected to P_{tot}.

3.1.2 Delta in ASDEX Upgrade for Negative Triangularity Shots

The typical negative triangularity shape in the previous chapter is a perfectly flipped "D" seen in TCV, DIII-D, and simulations [Fig. 2.2]. However, in

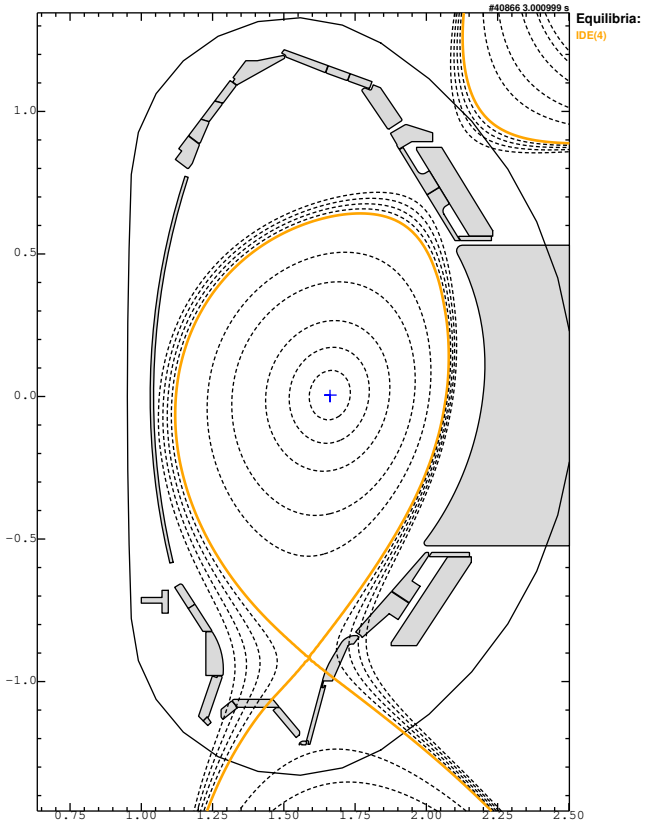

FIGURE 3.1: The cross-section of #40866. Negative triangularity shot of AUG shows a tilted reversed D shape.

ASDEX Upgrade, the same flipped "D" cannot be actualized because the shaping coils locates outside the vessel [Fig. 3.1]. This makes it challenging to push the plasma shaping in unconventional ways. Limitations in the maximum currents allowed in these shaping coils restrict the shaping capability towards more extreme NT configurations. Equally important, only a limited region of the plasma cross-section, the divertor, is designed to withstand high heat loads. The AUG divertor is designed and optimized for PT plasma configurations. NT experiments have been conducted on ASDEX-U since 2019 [Happel et al., 2022], gradually pushing the plasma to a more negative delta and to higher

plasma current by 2022. Fig. 3.2 shows time traces of the upper triangularity

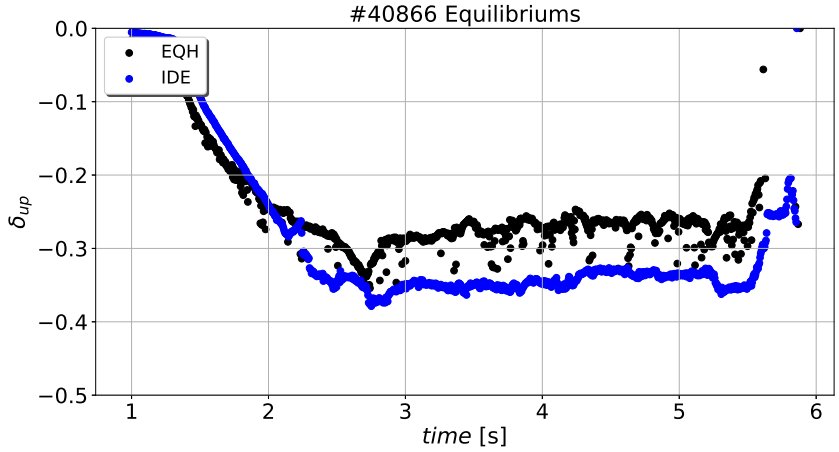

FIGURE 3.2: #40866 upper triangularity δ_{up} by different equilibrium codes. EQH and IDE are compared.

calculated with EQH and IDE. It can be seen that they agree well in the beginning until 2 s. However, they significantly deviate in the flat-top phase 2.7 s to 5.6 s. In addition to delta, other quantities deviate as well.

3.2 Heat Flux Profiles

With the IR camera and THEODOR code described in the previous chapter, the heat flux profile striking the divertor tile can be calculated. The analyzed discharges in NT do not exhibit large ELMs typically shown in H-mode scenarios but have high-frequency transients, with frequencies in the range of multiple 10 kHz. In the case of discharges with large and low frequent ELMs, a distinguishing between inter-ELM and intra-ELM can be performed in the IR analysis. On the other hand, in NT discharges, the transients occur faster than the IR camera's time resolution. Thus, before further processing, the IR profiles are time-averaged by ten previous and following time points, corresponding to 32 ms (1.6 ms per frame, 625 Hz). These time-averaged profiles are fitted using Eq. 2.14 to extract the physics quantities, such as the power fall-off length.

3.2.1 Heat Flux Profile on Outer Divertor Tile 2

For the NT shot, the strike point is not on a flat full tungsten tile (outer divertor tile 1) like PT but on a curved tungsten-coated carbon tile (outer divertor tile 2) [Fig. 3.3]. In the case of tile 1, it is possible to calculate the profile by designating two points and interpolating the points on a straight line between the two points[Fig. 2.9 (right)]. However, for the curved shape of tile

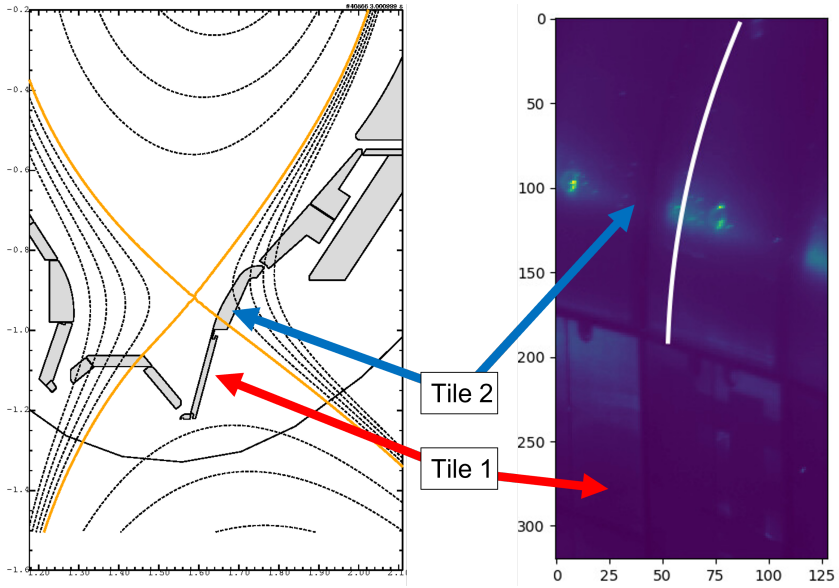

FIGURE 3.3: The poloidal cross-section of magnetic field and the narrow view of IR camera system for negative triangularity #40866. (left) The solid line (orange) is separatrix, and outer divertor tiles are indicated. In addition, the flux expansion of negative triangularity is shown. (right) The numbers in the axes are pixels.

2, it is necessary to apply a curve rather than a straight line. Therefore, heat flux calculation in NT is possible by extracting the curve's points by creating a function of the curve. First, to get the curve function, an image of the curve is drawn by hand using a tablet, and the image is converted to data points through a program called Engauge Digitizer [Mitchell et al, 2022], which creates data points from the image. After the image is converted to data points, the function is created by fitting. In addition, to calculate heat flux on tile 2, the angle of the IR camera is adjusted so that more parts of tile2 can be seen, and the frame size is adjusted to measure with higher time resolution. As a result of calculating with the corresponding curve, there are photons fluxes reflected from other tile or baffle to the IR camera at the beginning of tile2. The first 10 points are removed for more accurate calculations [Fig. 3.4] because their heat flux is not from the examining tile. Also, it shows an example of a well-calculated profile. It can be seen that the data points and the fit are almost identical.

3.2.2 Filters to Exclude Invalid Profiles

However, not all time points can be used. Causes for invalid time points are, among others, (i) low signal, (ii) strike line being to close the tile edges, (iii) hot spots, (iv) fitting failed, (v) broadening factor S larger than fall-off length λ_q, and (vi) other plasma parameters is invalid.

Fig. 3.5 presents examples of disregarded time points which is the case of (iii) and (i)(ii). The hot spots exhibit an increased temperature response due

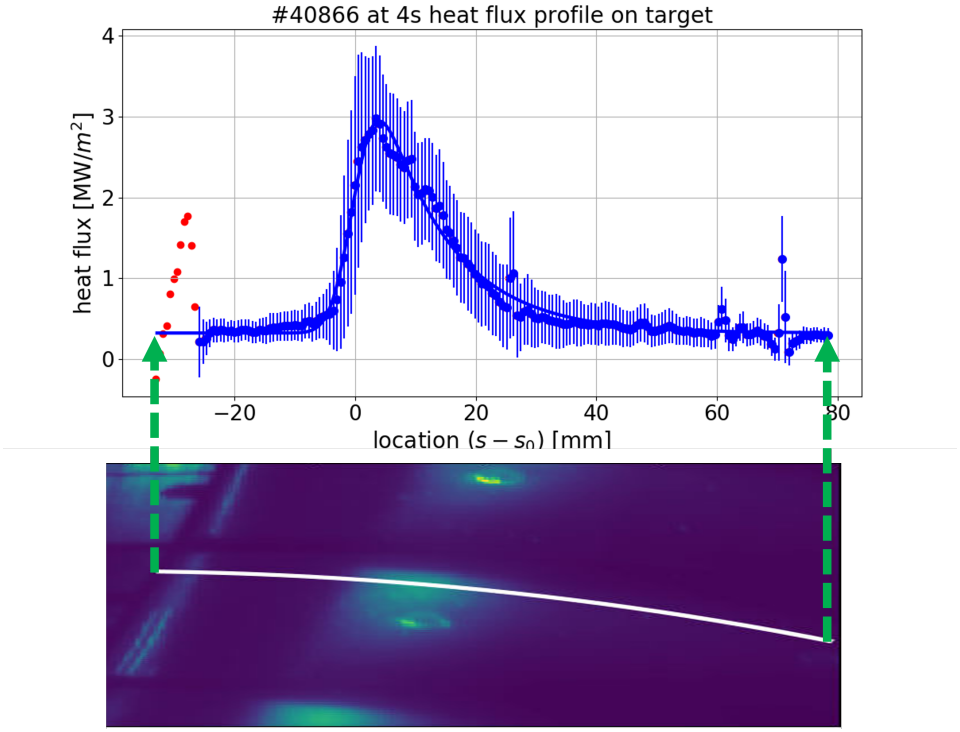

FIGURE 3.4: The heat flux calculation of #40866 and fitting by Eq. 2.14 with 1D curve on divertor tile 2. (top) The q profile at 4s of #40866. red dots are excluded for accurate fitting. (bottom) cropped image of the narrow view frame of #40866. At the edge of tile2, there are reflections from other tiles. The white solid line is the 1D curve used in the calculation.

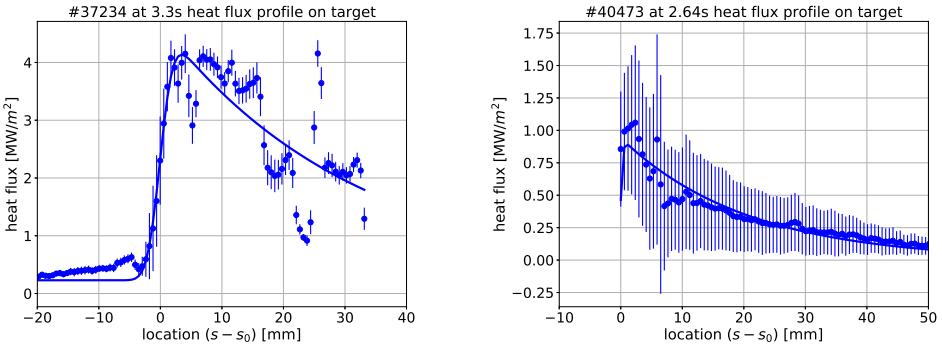

FIGURE 3.5: examples of invalid time points. (left) profile of existing hot spots. (right) a case of the strike line being too close to the edge and low signal.

to the lower thermal contact. With this, the calculation shows higher heat flux, which assumes a homogeneous surface. The low signal is often shown together with case (ii) because it happens early in discharge, and flux has not arrived at tile2. Another filter is applied when the divertor broadening factor is too large compared to λ_q. As shown in [Sieglin, 2014], the λ_q estimate

becomes uncertain even at a low noise level when S has a larger value than λ_q. Thus, there are some time points where the gained value is not trustable. In addition, time points with unreliable equilibrium reconstruction are excluded. These include the ramp-up phase before the final equilibrium is reached as well as time points after the current flat-top and main heating phase. Filters are applied to find plausible data points. Thus, the number of data points is significantly increased compared to hand-picking individual time points. Based

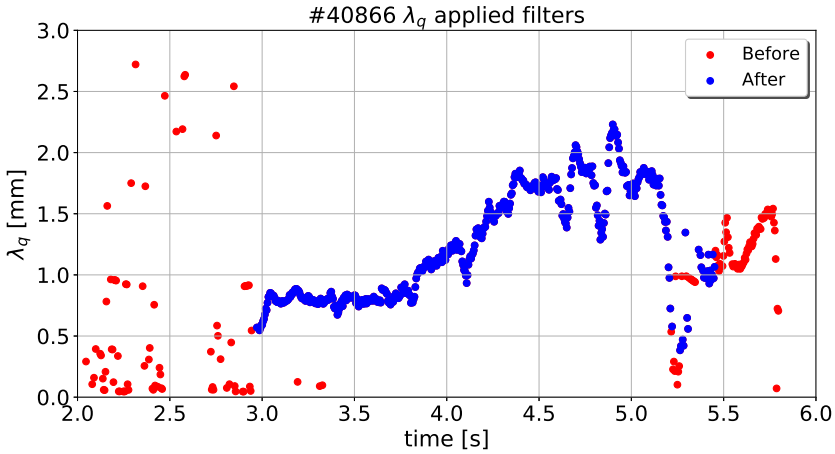

FIGURE 3.6: The time evolution of fall-off length in #40866. Red dots are neglected in final data acquisition.

on these filters, it was possible to obtain reliable data for most of the discharge duration, as shown in Fig. 3.6.

Chapter 4

Power Exhaust in Negative Triangularity

In this chapter, the heat flux data are compared to plasma parameters and between scenarios. The main manipulated variables within the NT data set are the two drift directions and the plasma current amplitudes. First, the heating power amount shows a strong influence on the heat flux variables. The heating power as a parameter should be considered the total amount, regardless of methods, including ohmic heating, because it has too many differences between discharges. Next, comparisons only in NT are conducted using different plasma currents and drift directions. Further, the effect of the varying delta is checked with two other regimes, which are typically operated in PT at similar heating power levels. In favorable drift direction, the EDA H-mode and in unfavorable, the I-mode are used to compare scenarios or the influence of the delta. Also, comparisons with scaling law predictions, as well as the heuristic drift-based model, are presented.

4.1 Heating Power Dependence

The first thing to check in the obtained data was to see the change in λ_q and the change in plasma parameters with time. Plasma parameters, stored energy, density, temperature, poloidal magnetic field, safety factor, pressure, and heating power, are compared with λ_q. Among them, the heating power showed the highest correlation, and in the model introduced earlier [ref. Section], it is considered the primary variable. Fig. 4.1 shows λ_q correlation to the heating power. Among the NT shots, #40866 has the least scattering heat flux data. After 3.7 s, it shows that as the heating power (blue dots) increases, the fall-off length (red dots) also increases. On the other side, #38733 shows a less obvious despite steps in heating power. However, it presents other relation from eq. 2.17 between heat flux values in Fig. 4.2. As the heating power increases, the value of q_{max} increases. This is consistent with an about fixed ratio of power impinging on the outer divertor target and input power. In this data

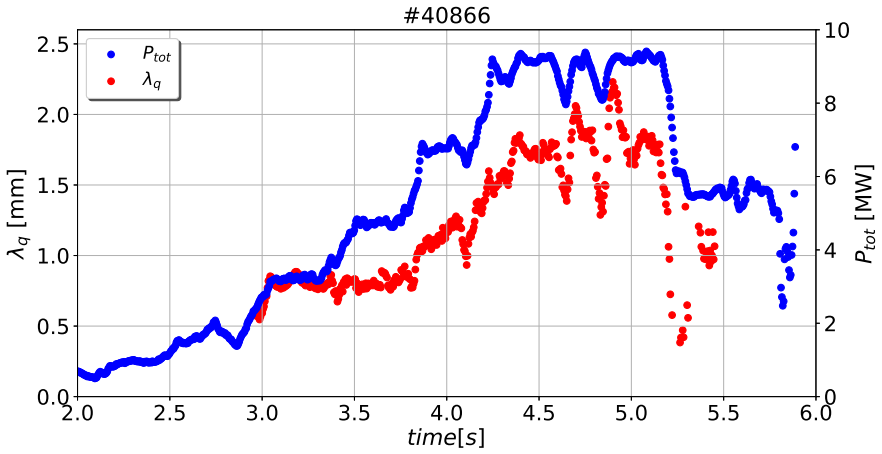

FIGURE 4.1: Time traces of power fall-off length λ_q (red) and total input power P_{tot} (blue) for #40866.

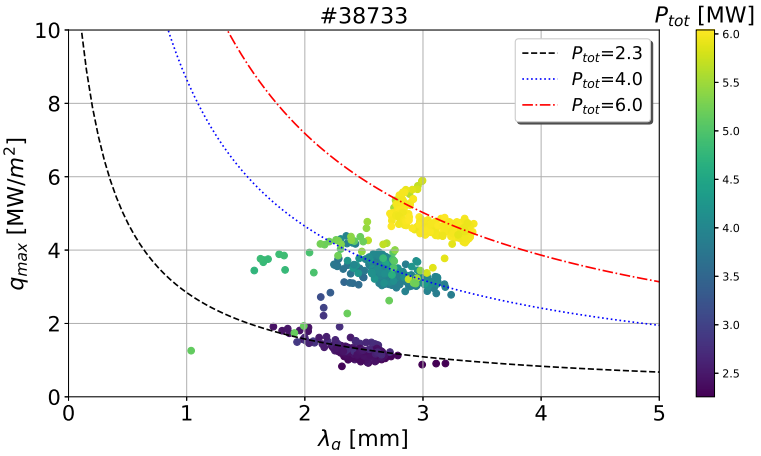

FIGURE 4.2: Peak divertor power load q_{max} depending on the power fall-off length λ_q for #38733.This discharge has unfavorable drift direction and plasma current of Ip=400 kA. Color-coded is the total input power P_{tot}. Each line represents eq. 2.12 with $P_{div} = (0.3 \pm 0.1)(P_{tot} - P_{rad})$

set, it is about $P_{div}^{outer}/P_{sep} = 0.3 \pm 0.1$. The variation of λ_q for each power step is anti-correlated to the peak power level. In the case of λ_q, even when the heating power is the same and increased, they are bounded between 1.8 mm and 3.5 mm. Otherwise, in the case of q_{max}, it showed a tendency to increase with higher heating power. Therefore, comparison and analysis were carried out using the heating power as the main parameter also in the later section.

4.2 Plasma Current Dependence

The poloidal magnetic field is one of the main scaling parameters for multi-machine scaling laws of λ_q [Eich et al., 2013].

$$B_{pol}^{avg} = \frac{\mu_0 I_p}{2\pi a} \frac{1}{\sqrt{(1+\kappa^2)/2}} \tag{4.1}$$

B_{pol}^{avg} is averaged poloidal magnetic field where μ_0 permeability of vacuum, I_P plasma current, a minor radius, and κ elongation. For a single machine, the plasma current is the dominant quantity in B_{pol}. In the NT campaign at AUG, three different plasma currents, 400, 600, and 800 kA, were realized. Fig. 4.3 shows the power fall-off length depending on the total input power in

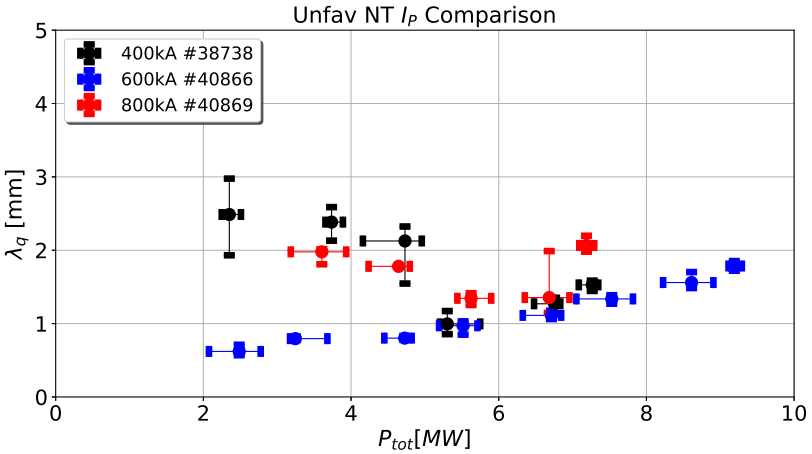

FIGURE 4.3: power fall-off length λ_q depending on total input power P_{tot} for unfavorable drift direction. Color-coded is the plasma current amplitude. The bar is also used here, indicating 25% to 75% of the data, and the centered dot is the median value. Each data point with bars includes a heat flux data range of each 1 MW.

unfavorable drift direction for all three plasma currents. The first three dots in 400 kA (black) and two dots in 800 kA (red) are in the early phase of heating and equilibrium, but those have valid heat profiles and have passed through the filters. While the values deviate at low input power (< 5 MW), they align in the range of 5-7 MW, regardless of the current. No clear dependence on plasma current can be found in this data set. The same result can also be found in the favorable drift direction. in Fig. 4.4. No deviation between both available plasma current values is observed for the entire range of heating power.

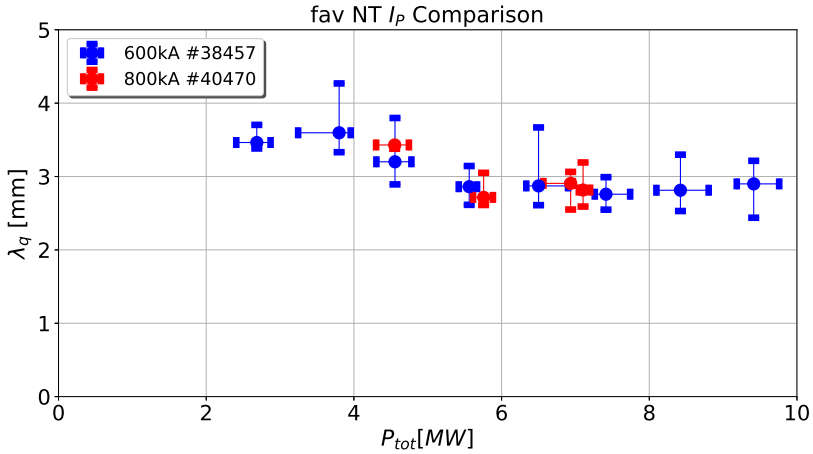

FIGURE 4.4: power fall-off length λ_q depending on total input power P_{tot} for favorable drift direction. The bar indicates 25% to 75% of the data, and the centered dot is the median value. Each data point with bars includes a heat flux data range of each 1 MW. Because of the IR camera failure by high coil current, the 800 kA shot has less number of data.

4.3 Drift Direction Dependence

In the previous section, Figures A and B, the two drift directions showed a large difference in λ_q. In addition, the plasma drift direction has an essential role in the L-H transition (Section. 2.3.2). For the NT reactor, one might want to choose the unfavorable drift direction to ensure L-mode operation. For this reason, in AUG, unfavorable drift experiments were conducted. Fig 4.5 shows the power fall-off length depending on the total input power for both drift directions. It can be seen that for both (top) 600 kA, as well as (bottom) 800 kA, smaller values in the unfavorable direction are measured. Besides, there is no significant change in fall-off length by changing the heating power except for unfavorable drift with $I_P = 600$ kA shot.

4.4 Scenario Comparisons

In order to quantify the power exhaust capability of NT plasmas, a comparison with other regimes is performed. To match as many of the same plasma parameters as possible between scenarios, comparison groups have to have a lower single null configuration, I_P=600 kA or 800 kA, the same magnetic field strength, 2.5 T, and a similar range of heating power. In addition, not only to meet the conditions but also for the IR data, shots should avoid type I ELMs. Typical L-mode discharges at ASDEX Upgrade in positive triangularity have a too-low heating power and density compared to NT. Accordingly, EDA and I-mode shots have many overlapping ranges of parameters, especially one with favorable drift, and the other with unfavorable drift configuration. Figure 4.6

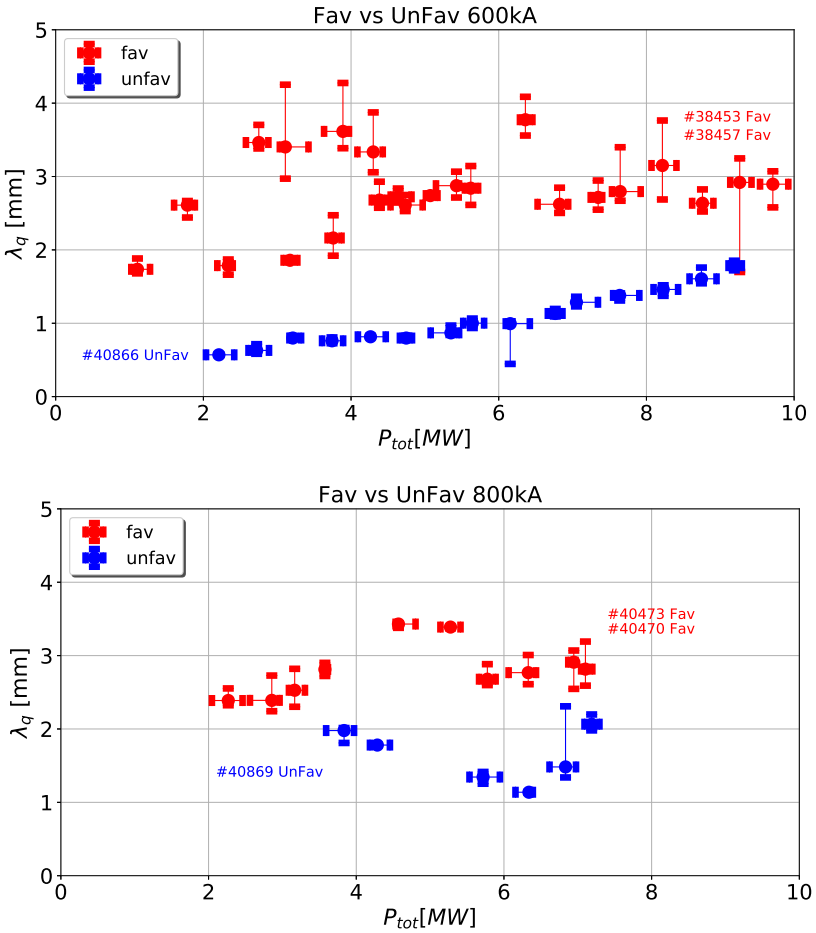

FIGURE 4.5: power fall-off length λ_q depending on total input power P_{tot} for I_P=600 kA and 800 kA. the error bars are used for clearance, indicating the bottom 25% and the top 75%, and the dots are median values of each 0.5 MW range of heating power. Red and blue represent favorable (-2.5 T) and unfavorable (2.5 T) drift directions, respectively. (top) I_P=±600 kA (bottom) I_P=±800 kA. fewer data points are available due to limitations in the IR camera set-up, failing at very high shaping coil currents reached around 3.8 s at 800 kA.

shows λ_q depending on the upper triangularity. The three plasma scenarios are color-coded. The NT data points exhibit a significant variation. The difference between the two groups of points is the drift direction, with the lower values in unfavorable configuration, as presented in section 4.3. In the case of I_P is 600 kA, λ_q of NT is smaller than that of EDA (favorable drift) and I-mode (unfavorable drift). However, for I_P=800 kA, the fall-off length is nearly the same as with the opponents except for one point in EDA which has $\lambda_q > 5$ mm.

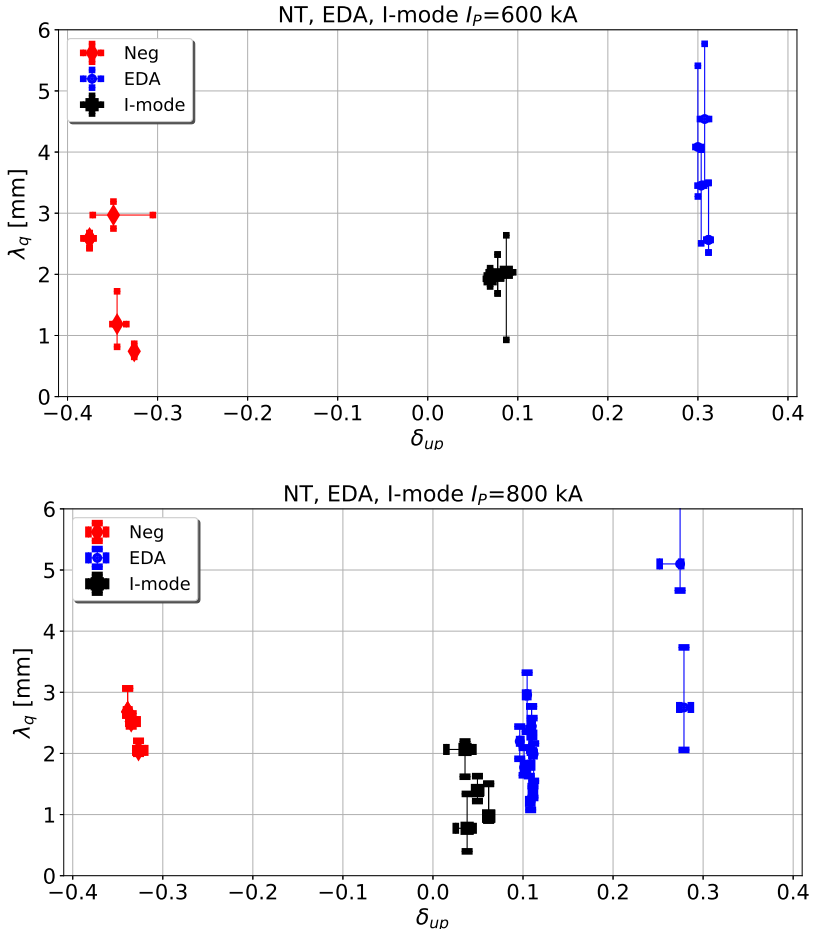

FIGURE 4.6: power fall-off length λ_q depending on upper triangularity δ_{up} for I_P=600 kA and 800 kA.The error bar is also used here, indicating 25% to 75% of the data, and the centered dot is the median value independent from the heating power. Each color represents scenarios, NT (red), EDA(blue), and I-mode(black).

4.5 Fall-Off Length Predictions Comparisons

Comparisons were made based on actual measured data so far. In this section, model values were obtained and compared using the previous results and data. In this thesis, NT λ_q values are measured only in AUG. Therefore, among the various published scaling laws, the comparison is performed with the ones containing AUG data. These are the multi-machine scaling law [Eich et al., 2013] and Eq. 2.32, H-mode scaling for JET and AUG [Eich et al., 2011], Eq. 2.33 and L-mode scaling law for AUG [Sieglin et al., 2016], Eq. 2.34. Fig. 4.7 presents the comparison between multi-machine scaling law and measured λ_q. In the case of the favorable drift shots, the data shows slightly larger values than the regression prediction, although within the uncertainty margin of this scaling. On the other hand, as shown in the previous section, unfavorable drift shots have a significantly smaller λ_q compared to favorable drift shots. The scaling

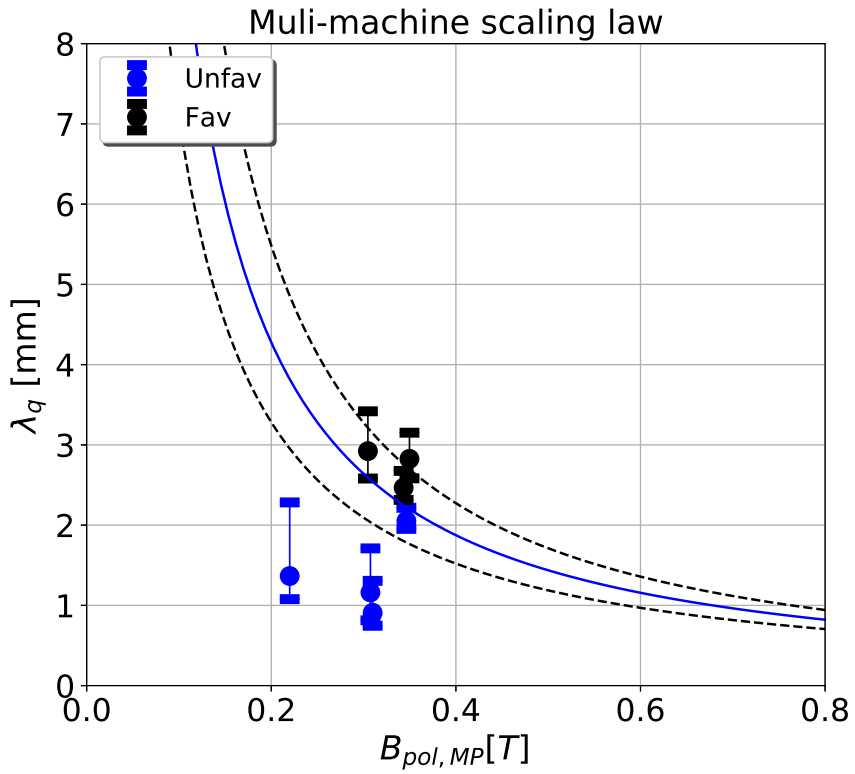

FIGURE 4.7: Poloidal magnetic field at the outer midplane versus power fall-off length λ_q. The regression model is expressed as a solid line with an error(dashed). blue and black dots are measured unfavorable drift NT and favorable, respectively.

law does not predict a change in drift direction, and hence the measured values are well below the prediction. It is noted that unfavorable drift direction is not routinely studied for H-mode plasmas, and the scaling law was exclusively containing data points with favorable drift direction. The NT λ_q does not show a noticeable dependence on the B_{pol}, although it has to be noted that the realized range in B_{pol} is small due to the single machine being studied here. Nevertheless, for further comparisons, the two investigated plasma currents are plotted in individual figures to account for the dependence on q_{cyl} in these scaling laws. Fig. 4.8 shows the same data set as Fig. 4.5 for I_P =600 kA. Added are the scaling law predictions for the L- and H-mode experimental scaling laws as well as for the HD-Fav model (heuristic drift model for favorable configuration) in the formatting as used in [Eich et al., 2011] (Eq. 2.43. Similar to the multi-machine scaling, the absolute size of λ_q for favorable configuration agrees well with all scaling laws. The most significant difference between the H-mode and L-mode scaling laws is the different signs in the power dependence. While the L-mode scaling predicts a decrease of λ_q with increasing power, the H-mode scalings predict an increase. It can be seen that at low P_{tot}, L-mode scaling is closer to the measured values, while at higher P_{tot}, the

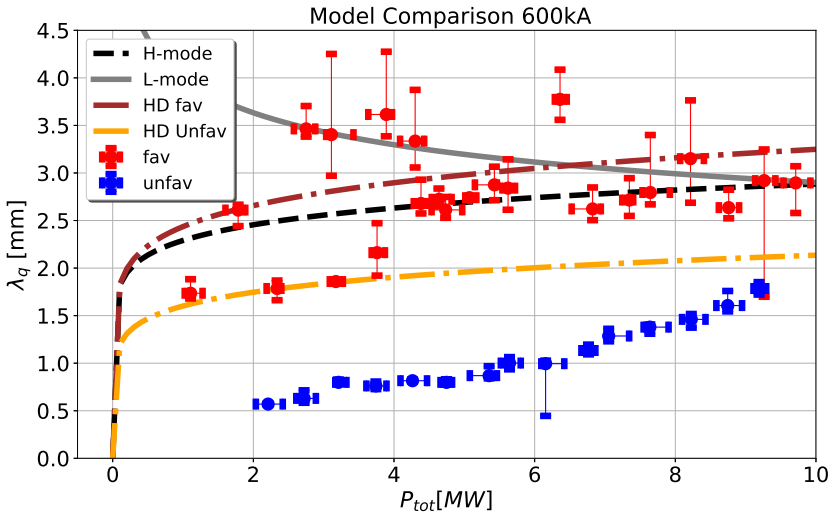

FIGURE 4.8: Predictions of regression models and heuristic model for plasma current 600 kA are added to Fig. 4.5. Legends in the figure indicate models by different colors and types of lines. HD-Fav stands for heuristic drift model for favorable configuration, and HD-Unfav is for unfavorable configuration.

HD-Fav has the closest prediction. On the other hand, the reversed field configuration does not match any of the models. This is similar to L-mode results at AUG [Faitsch et al., 2015]. In this study, the HD model was adjusted for unfavorable drift direction (see Section. 2.6.2). This HD-Unfav (heuristic drift model for unfavorable configuration) predicts lower values of about 2 mm, a reduction in the order of 1 mm. However, the measured data is even smaller than the adjusted scaling law. Fig. 4.9 is for I_P =800 kA. All shown scaling laws have an inverse dependence on the safety factor. Hence, the predictions are lower for 800 kA compared to 600 kA. However, the measured values do not change with the change in I_P, as shown in the section. 4.2. With this, the measured $lambda_q$ in favorable drift is larger than all scaling law predictions, except at low P_{tot} where the L-mode scaling is close to the measured values, similar to what was observed in Fig. 4.8 for the 600 kA shots. On the other hand, in unfavorable drift shots, the prediction of HD-Unfav is close to the measured values. they do not exhibit consistency for both configurations.

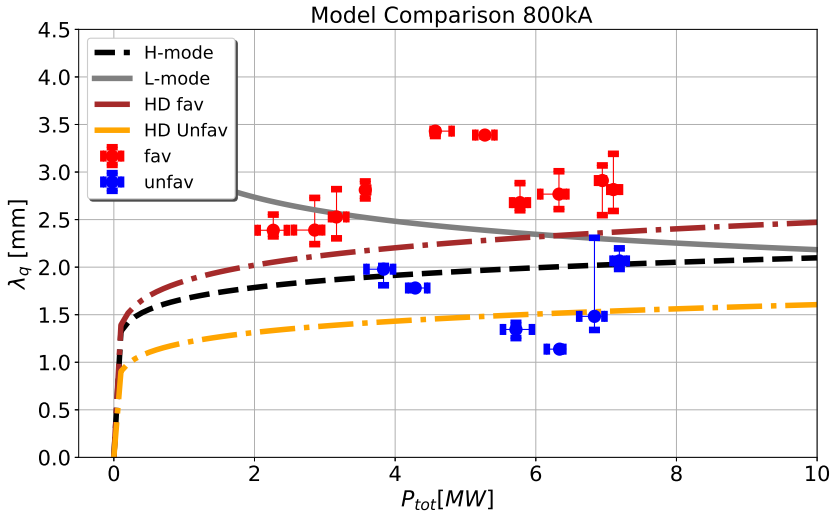

FIGURE 4.9: Predictions of regression models and heuristic model for plasma current 800 kA are added to Fig. 4.5. Legends in the figure indicate models by different colors and types of lines.

Chapter 5

Summary and Conclusions

In this thesis, the investigation of the power exhaust for ASDEX Upgrade in negative triangularity is reported. Even though power loads into the divertor are tolerable for existing devices, unmitigated power loads onto the divertor are not tolerable for future fusion reactors. In order to have a reliable and sustained operation in upcoming fusion devices, measures for reducing power loads onto the divertor have to be developed. As one of the alternatives, NT has recently attracted attention. The NT scenario wants to be operated in L-mode rather than H-mode. As a natural choice, the operation should be in unfavorable directions to increase the operational window. However, the power exhaust properties of this novel configuration are yet to progress. This thesis provides the first step for AUG in the investigation of the power fall-off length.

In this thesis, it is shown that the power fall-off length changes significantly with the drift direction. Namely, the power fall-off length is smaller in the unfavorable drift direction. It is speculated that this is an effect of the drifts in the SOL because global plasma parameters did not vary significantly between the shots with varying drift directions. In addition, the comparison with other ELM-free scenarios at similar input parameters showed NT has the same or smaller λ_q in AUG. There was no strong effect of δ on λ_q, but λ_q of NT was smaller than that of the stronger shaping of positive triangularity.

Several scaling laws introduced in this thesis showed that λ_q in favorable drift direction NT fits very well with the predictions. Conversely, λ_q in unfavorable configuration is clearly smaller than the various predictions. Among the scaling laws, the multi-machine scaling law has the closest agreement in fav drift. In other words, the measured λ_q still fits the multi-machine scaling law even for extreme shaping like negative triangularity.

The fall-off length of the unfavorable drift did not match with any model. Further, no scaling law considering triangularity is available. Future work will need to address both the effect of the drift direction as well as a possible de-

pendence on triangularity. However, only a limited range of NT values was realized in AUG. DIII-D and TCV conducted experiments with more extreme triangularity, so these experiments could be valuable data for future work to study such effects together with the data collected within this thesis.

From this thesis, it is evident that the power fall-off length cannot easily be transferred between drift directions and scenarios. The studies and design of potential future fusion devices based on the NT concept will need to consider that the power fall-off length might be significantly smaller than the primarily used scaling laws predictions based on measurements in favorable field H-mode.

Bibliography

[AUG webpage, 2022] AUG webpage (6st October 2022). *Diagnostics Description of the ASDEX Upgrade Infrared Thermography Systems.* `https://www.aug.ipp.mpg.de/~ircd/webpage/html-data/index.html` (Accessed: November 14, 2022).

[Coda et al., 2021] Coda, S., Merle, A., Sauter, O., et al. (2021). Enhanced confinement in diverted negative-triangularity l-mode plasmas in tcv. *Plasma Physics and Controlled Fusion*, 64, 014004.

[Eich et al., 2013] Eich, T., Leonard, A., Pitts, R., et al. (2013). Scaling of the tokamak near the scrape-off layer H-mode power width and implications for ITER. *Nuclear Fusion*, 53, 093031.

[Eich et al., 2011] Eich, T., Sieglin, B., Scarabosio, A., et al. (2011). Inter-ELM power decay length for JET and ASDEX Upgrade: Measurement and comparison with heuristic drift-based model. *Physical Review Letters*, 107, 215001.

[Eich et al., 2017] Eich, T., Sieglin, B., Thornton, A., et al. (2017). ELM divertor peak energy fluence scaling to ITER with data from JET, MAST and ASDEX Upgrade. *Nuclear Materials and Energy*, 12, 84.

[euro-fusion.org, 2011] euro-fusion.org (2011). *Tokamak Principle.* `https://www.euro-fusion.org/2011/09/tokamak-principle-2/?view=gallery-428` (Accessed: November 14, 2022).

[Faitsch, 2017] Faitsch, M. (2017). *Divertor Power Load Studies in ASDEX Upgrade and TCV.* PhD thesis, Ludwig-Maximilians-Universität München, München.

[Faitsch et al., 2018] Faitsch, M., Maurizio, R., Gallo, A., et al. (2018). Dependence of the L-Mode scrape-off layer power fall-off length on the upper triangularity in TCV. *Plasma Physics and Controlled Fusion*, 60, 045010.

[Faitsch et al., 2015] Faitsch, M., Sieglin, B., Eich, T., et al. (2015). Change of the scrape-off layer power width with the toroidal B-field direction in ASDEX Upgrade. *Plasma Physics and Controlled Fusion*, 57, 075005.

[Fischer et al., 2016] Fischer, R., Bock, A., Dunne, M., et al. (2016). Coupling of the flux diffusion equation with the equilibrium reconstruction at asdex upgrade. *Fusion Science and Technology*, 69, 526.

[Fischer et al., 2010] Fischer, R., Fuchs, C., Kurzan, B., Suttrop, W., and Wolfrum, E. (2010). Integrated data analysis of profile diagnostics at ASDEX upgrade. *Fusion Sci. Technol.*, 58, 675.

[fusionwiki, 2014] fusionwiki (12 June, 2014). *Tokamak geometry sketch*. `http://fusionwiki.ciemat.es/wiki/File:Geometry.png` (Accessed: November 14, 2022).

[Gil et al., 2020] Gil, L., Silva, C., Happel, T., et al. (2020). Stationary ELM-free h-mode in ASDEX upgrade. *Nuclear Fusion*, 60, 054003.

[Goldston, 2012] Goldston, R. J. (2012). Heuristic drift-based model of the power scrape-off width in low-gas-puff H-mode tokamaks. *Nuclear Fusion*, 52, 013009.

[Greenwald et al., 1999] Greenwald, M., Boivin, R., Bonoli, P., et al. (1999). Characterization of enhanced da high-confinement modes in alcator c-mod. *Physics of Plasmas*, 6, 1943.

[Haines et al., 2000] Haines, M., Lebedev, S., Chittenden, J., et al. (2000). The past, present, and future of z pinches. *Physics of Plasmas*, 7, 1672.

[Happel et al., 2022] Happel, T., PÃ¼tterich, T., Told, D., et al. (2022). Overview of initial negative triangularity plasma studies on the asdex upgrade tokamak. *Nuclear Fusion*.

[Herrmann et al., 1995] Herrmann, A., Junker, W., Guenther, K., et al. (1995). Energy flux to the ASDEX-Upgrade divertor plates determined by thermography and calorimetry. *Plasma Physics and Controlled Fusion*, 37, 17.

[ITER Physics Expert Group on Confinement and Transport et al., 1999] ITER Physics Expert Group on Confinement and Transport, ITER Physics Expert Group on Confinement Modelling and Database, and ITER Physics Basis Editors (1999). Chapter 2: Plasma confinement and transport. *Nuclear Fusion*, 39, 2175.

[Lampert et al., 2022] Lampert, M., Diallo, A., Myra, J. R., and Zweben, S. J. (2022). Internal rotation of elm filaments on nstx. *Physics of Plasmas*, 29, 102502.

[Loarte et al., 1999] Loarte, A., Bosch, S., Chankin, A., et al. (1999). Multi-machine scaling of the divertor peak heat flux and width for L-mode and H-mode discharges. *Journal of Nuclear Materials*, 266, 587.

[Loarte et al., 2003] Loarte, A., Saibene, G., Sartori, R., et al. (2003). Characteristics of type I ELM energy and particle losses in existing devices and their extrapolation to ITER. *Plasma Physics and Controlled Fusion*, 45, 1549.

[Luce, 2013] Luce, T. C. (2013). An analytic functional form for characterization and generation of axisymmetric plasma boundaries. *Plasma Physics and Controlled Fusion*, 55, 095009.

[Makowski et al., 2012] Makowski, M. A., Elder, D., Gray, T. K., et al. (2012). Analysis of a multi-machine database on divertor heat fluxes. *Physics of Plasmas*, 19, 056122.

[Marinoni et al., 2021a] Marinoni, A., Austin, M., Hyatt, A., et al. (2021a). Diverted negative triangularity plasmas on diii-d: the benefit of high confinement without the liability of an edge pedestal. *Nuclear Fusion*, 61, 116010.

[Marinoni et al., 2009] Marinoni, A., Brunner, S., Camenen, Y., et al. (2009). The effect of plasma triangularity on turbulent transport: modeling TCV experiments by linear and non-linear gyrokinetic simulations. *Plasma Physics and Controlled Fusion*, 51, 055016.

[Marinoni et al., 2021b] Marinoni, A., Sauter, O., and Coda, S. (2021b). A brief history of negative triangularity tokamak plasmas. *Reviews of Modern Plasma Physics*, 5, 6.

[Marinoni et al., 2018] Marinoni et al. (November 22, 2018). *High Confinement in Negative Triangularity Discharges in DIII-D.* `https://nucleus.iaea.org/sites/fusionportal/Shared%20Documents/FEC%202018/fec2018-preprints/preprint0391.pdf` (Accessed: November 14, 2022).

[Mitchell et al, 2022] Mitchell et al (November 14, 2022). *Engauge Digitizer Software.* `http://markummitchell.github.io/engauge-digitizer` (Accessed: November 14, 2022).

[Moret et al., 1997] Moret, J.-M., Franke, S., Weisen, H., et al. (1997). Influence of plasma shape on transport in the TCV tokamak. *Phys. Rev. Lett.*, 79, 2057.

[Neu et al., 2002] Neu, R., Dux, R., Geier, A., et al. (2002). Impurity behaviour in the ASDEX upgrade divertor tokamak with large area tungsten walls. *Plasma Physics and Controlled Fusion*, 44, 811.

[Nille et al., 2018] Nille, D., von Toussaint, U., Sieglin, B., and Faitsch, M. (2018). Probabilistic inference of surface heat flux densities from infrared thermography. In *Bayesian Inference and Maximum Entropy Methods in*

Science and Engineering, pages 55–64, Cham. Springer International Publishing.

[Planck, 1900a] Planck, M. (1900a). Über eine Verbesserung der Wienschen Spektralgleichung. *Deutsche Physikalische Gesellschaft, Verhandlungen*, 2, 202.

[Planck, 1900b] Planck, M. (1900b). Zur Theorie des Gesetzes der Energieverteilung im Normalspektrum. *Deutsche Physikalische Gesellschaft, Verhandlungen*, 2, 237.

[Pochelon et al., 1999] Pochelon, A., Goodman, T., Henderson, M., et al. (1999). Energy confinement and MHD activity in shaped TCV plasmas with localized electron cyclotron heating. *Nuclear Fusion*, 39, 1807.

[Ryter et al., 2016] Ryter, F., Fischer, R., Fuchs, J., et al. (2016). I-mode studies at asdex upgrade: L-i and i-h transitions, pedestal and confinement properties. *Nuclear Fusion*, 57, 016004.

[Schneider et al., 2000] Schneider, W., McCarthy, P., Lackner, K., et al. (2000). ASDEX Upgrade MHD equilibria reconstruction on distributed workstations. *Fusion Engineering and Design*, 48, 127.

[Sieglin et al., 2016] Sieglin, B., Eich, T., Faitsch, M., et al. (2016). Investigation of scrape-off layer and divertor heat transport in ASDEX Upgrade L-mode. *Plasma Physics and Controlled Fusion*, 58, 055015.

[Sieglin et al., 2015] Sieglin, B., Faitsch, M., Herrmann, A., et al. (2015). Real time capable infrared thermography for ASDEX Upgrade. *Review of Scientific Instruments*, 86, 113502.

[Sieglin, 2014] Sieglin, B. A. (2014). *Experimental Investigation of Heat Transport and Divertor Loads of Fusion Plasmas in All Metal ASDEX Upgrade and JET*. Dissertation, Technische UniversitÃ¤t MÃ¼nchen, MÃ¼nchen.

[Snyder et al., 2002] Snyder, P. B., Wilson, H. R., Ferron, J. R., et al. (2002). Edge localized modes and the pedestal: A model based on coupled peeling-ballooning modes. *Physics of Plasmas*, 9, 2037.

[Stroth, 2018] Stroth, U. (2018). *Plasmaphysik*. Springer Spektrum Berlin, Heidelberg.

[Wagner et al., 1985] Wagner, F., Bartiromo, R., Becker, G., et al. (1985). Experimental evidence for neoclassical ion transport effects in the h-transition of ASDEX. *Nuclear Fusion*, 25, 1490.

[Wagner et al., 1982] Wagner, F., Becker, G., Behringer, K., et al. (1982). Regime of improved confinement and high beta in neutral-beam-heated divertor discharges of the ASDEX tokamak. *Phys. Rev. Lett.*, 49, 1408.

[Wesson and Campbell, 2011] Wesson, J. and Campbell, D. (2011). *Tokamaks*. International Series of Monographs on Physics. OUP Oxford.

[Whyte et al., 2010] Whyte, D., Hubbard, A., Hughes, J., et al. (2010). I-mode: an h-mode energy confinement regime with l-mode particle transport in alcator c-mod. *Nuclear Fusion*, 50, 105005.

[Zohm, 1996] Zohm, H. (1996). Edge localized modes (ELMs). *Plasma Physics and Controlled Fusion*, 38, 105.